UNIVERSITY
OF TRENTO - Italy
DEPARTMENT OF INDUSTRIAL ENGINEERING

XXV cycle

Doctoral School in Materials Science and Engineering

Production of a nanostructured copper by Spark Plasma Sintering

Saliou Diouf

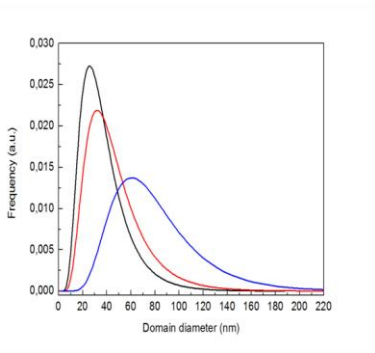

April 2013

Production of a nanostructured copper by Spark Plasma Sintering

Saliou Diouf

Tutor:
Prof. Alberto Molinari

Approved by:

Prof. Alberto Molinari, Advisor
Dipartimento di Ingegneria Industriale
Università degli studi di Trento*, Italia.*

Prof. Claudio Migliaresi,
Dipartimento di Ingegneria Industriale
Università degli studi di Trento, Italia.

Ph.D. Commission:

Prof. Pranesh Aswath,
Department of Materials Science and Engineering and Mechanical and Aerospace Engineering
University of Texas Arlington, USA.

Prof. Orfeo Sbaizero,
Dipartimento di Ingegneria ed Architettura
University degli studi di Trieste, Italia.

Prof. Arthur J. Coury,
Coury Consulting Service
154 Warren Avenue Boston, MA 02116 (USA).

University of Trento,
Department of Industrial Engeneering

April 2013

University of Trento - Department of Materials Science and Engineering

Doctoral Thesis

Saliou - 2013
Published in Trento (Italy) – by University of Trento

ISBN: 978-88-8443-472-2

To my parents, my wife Salimata and my daughter Fatima

Abstract

The aim of the present PhD work is the study of the production of a nanostructured copper by Spark Plasma Sintering.

The nanostructured powder was produced by cryomilling an atomized powder, using a ball-to-powder ratio of 30:1 for 8h; it has a mean grain size of 19±2 nm and shows quite a high thermal stability, as shown by a DSC investigation.

The influence of temperature, particle size, pressure on the densification and sintering mechanisms as well as that of heating rate and holding time on the structural evolution has been investigated. Particle rearrangement, local deformation, bulk deformation and sintering are the SPS mechanisms occurring successively during the sintering process of the atomized copper. These mechanisms are enhanced by the peculiar heating mechanism in SPS, and the surface overheating above the melting temperature in the contact regions has been demonstrated. In the cryomilled powder, sintering occurs at much lower temperature than in the atomized powder, due to effect of the high density of structural defects on the mass transport phenomena responsible for neck growth.

The increase in heating rate tends to promote a bimodal grain size distribution (both nanomentric and ultrafine grains) while an increase in holding time increases grain size slightly. A promising combination of strength and ductility was measured on tensile specimens produced under selected conditions, and a dimpled fracture morphology was observed.

.

Table of contents

Chapter I
Introduction.....3

Chapter II
Spark plasma sintering (SPS) 5

2.1. The process parameters.....7

2.1.1. *The electrical current*.....7

2.1.2. The meaning of temperature.....9

2.1.3. The applied pressure 10

2.1.4. The heating rate 11

2.1.5. The holding time.....12

2.2. SPS of nanostructured materials *13*

2.3. Improvement of the mechanical properties by bimodal grain size distribution *14*

Chapter III
Experimental procedure 18

3.1. The atomized copper powder *18*

3.2. Cryomilling.....*18*

3.3. Spark Plasma Sintering.....*19*

3.4. Characterization procedures *20*

Chapter IV

Results and discussion.....22

4.1. The atomized copper powder 22

4.1.1. A DOE study of the effect of temperature, pressure and particle size 22

4.1.2. The densification and sintering mechanisms.....35

4.1.3. The confirmation of the surface melting of the particles.....48

4.1.4. Summary... 52

4.2. The cyomilled copper powder 54

4.2.1. Grain size and dislocation density.....54

4.2.2. Thermal stability.....55

4.2.3. Contamination and degassing behaviour..... 63

4.3. SPS of the cryomilled copper 66

4.3.1. A DOE study of the effect of temperature, pressure ans particle size 66

4.3.2. The effect of the nanostructure on densification and sintering mechanisms.....74

4.3.3. Influence of heating rate on grain size.....80

4.3.3.1. Applying only an initial pressure P_i 80

4.3.3.2. Applying final pressure at 900°C.....85

4.3.4. Tensile properties 91

4.3.5. Summary 96

Conclusions.....99

Publications 102

Bibliography.....103

Acknowledgements 111

Chapter I

Introduction

The production of relatively significant quanties of nanostructured metallic materials may be possible through the use of mechanical milling procedures (Suryanarayana, 2001). Cryomilling is a mechanical milling involving the immersion of the material to be milled in liquid nitrogen (-196°C) and using the milling time, ball-to-powder ratio, the balls dimension etc. as the processing parameters (Luton M. J., 1988; Perez R.J., 1998; Zhou F., 2003). The suppression of the annihilation of dislocations giving rise to a high dislocation density, the reduction of oxidation reactions due to the nitrogen environment and the shorter milling time are among the major advantages of cryomilling over conventional milling processes to achieve desirable characteristics of nanostructured metallic materials.

The large volume fraction of the atoms residing in the grain boundaries makes the nanostructured materials behavior significantly different from the coarse-grained polycrystalline counterparts (Suryanarayana C., 2000; Gleiter, 2000). This unique characteristic which is due to the small grain size lead to an increased in strength of these materials making them highly attractive. However, although they have a high yield strength (Valiev R. Z., 2000), the drawback associated with nanostructured materials is their reduced toughness along with their limited ductility of only a few percent of uniform ductility (Siegel R.W., 1995; Koch C.C., 1999; Grosdidier T., 2010 ; Ma, 2003). Over time significant efforts have been undertaken to achieve a relatively high ductility while maintening high strength (Hayes R.W., 2001; Lee Z., 2003).

To take advantage of the unique properties provided by nanocrystalline materials, the cryomilled powder have to be fully densified without totaly losing the nanostructure. Such a consolidation is much demanding since the use of a sintering technology along with a clear understanding of the consolidation process and its interaction with the nanostructured materials become a prerequisite step by which a highly dense bulk nanostructured metallic material can be obtained. The cleaning of

the particle surface, the breaking of the oxide layer and the enhancement of the mass transport between particles, resulting in a short sintering time, make Spark Plasma Sintering (SPS), described in chapter 2, a suitable technique.

In the specific case of nanostructured powders obtained by ball milling, the grain size decreases with particle size (Molinari A., 2010) .Consequently, the finer particles have a higher resistance to deformation than the coarse ones and are exposed to different local temperatures during SPS due to the different electrical resistance of the contact areas (Song X., 2006) A controlled densification of a nanostructured powder, to obtain a full density material with limited grain growth, requires the knowledge of the effect of particle size on densification.

A preliminary work was carried out using as-atomized powders to eliminate the effect of the different resistance to deformation provided by the different grain size (chapter 4). Copper was used as a “simple” metal and since, copper oxide does not seem to have no big effect on the consolidation mechanism as pointed out by Ritasalo et al. (Ritasalo R., 2010) considering an average particle size of 410 nm at 600°C with 100 MPa for 6 min, they came up with very good mechanical properties despite of the high Cu_2O-content.

The main goal of this PhD work is to produce a bimodal size distribution bulk copper material through a two step process: cryogenic milling and consolidation by SPS and by controlling heating..

Chapter II

Spark plasma sintering

Spark plasma sintering (SPS) is a recent pressure assisted sintering technique characterized by a fast heating rate, short sintering time and a relatively low sintering temperature. These characteristics result in a low heat input and make SPS a promising technique in producing highly dense materials with controlled microstructure. The main difference of the SPS in comparison to conventional hot pressing sintering techniques is that both the graphite die and the sample loaded inside it are heated by Joule effect of an applied dc current. Figure 1 shows a schematic of the SPS system which comprises a machine with vertical single-axis pressurization mechanism, specially designed punch electrodes incorporating water coller, a water-cooled vacuum chamber, a vacumm/air/argon-gas atmosphere control mechanism, a special sintering DC-pulse generator, a cooling water control unit, a position measuring unit, a temperature measuring unit, an applied pressure display unit and various interlock safety units (M.Tokita)

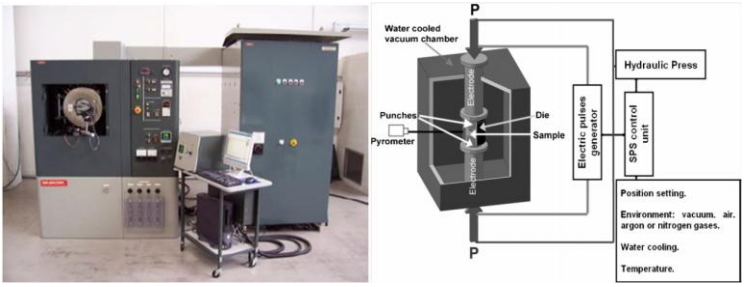

Figure 1: DR.SINTER 1050 system (left) and a schematic of the SPS system (Hungría T., 2009) (right)

The sintering temperature controle is made possible through the setting of the holding time, ramp rate, pulse duration, and pulse current and voltage.

The advantage of this method over the conventional ones (Langer J., 2009), lays in minimizing changes of the starting microstructures of the powder (Lu, 2008; Zúñiga A., 2006; Munir Z. A., 2006) (Lu, 2008; Zúñiga A., 2006; Munir Z. A., 2006) due to low heat input, and this is of great interest in processing metastable materials, as the nanostructured powders. The simultaneous application of pressure and pulsed continuous current (Mamedov, 2002; Orrù R., 2009) characterizing spark plasma sintering (SPS) and subsequently the fast heating rate attainable within a short sintering time makes it a suitable procedure by which highly dense bulk nanostructured metallic powders (Omori, 2000; Libardi S., 2007; Srinivasarao B., 2008) can be obtained with limited grain growth.

However, the complexity of the involved phenomena during the sintering process such as the generation of spark discharge at the gaps and the contact points of conductive particles, joule and electron field diffusion effects makes SPS a still not fully understood sintering process (Groza J. R., 2001). An analysis of the significant features of SPS has been published by Munir et al. (Munir Z. A., 2006) highlighting the influence of the high heating rate, of the application of pressure and of the current on consolidation and synthesis of materials. The discussion on the formation of a plasma, as proposed by Tokita (Tokita, 1999), is still open (Munir Z. A., 2006) , even if the recent paper of Hulbert et al. (Hulbert D. M., 2009) gives an experimental evidence of the absence of plasma during SPS.

These phenomena are both SPS parameters and materials dependant. Over years many attempts through mathematical modeling and experimental have been made to better understand the the effect of both SPS parameters and sample's material on the consolidation process. In the following a review of some recent publications will be presented on the effect of process parameters on the mechanisms of SPS.

2.1. The SPS parameters

The success of the SPS process arise from how effective it is on the material being processed. Chen et al. (Chen X.J., 2004) found out that SPS significantly reduces the grain boundary resistivity through the reduction of impurity segregation at grain

boundaries. This results in the cleaning of grain boundaries (Risbud S.H., 1994) and the limitation of drawback from impurities in SPS as well as the improvement of the bonding quality (Srinivasarao B., 2009) conversely to the conventional sintering processes. Such an advantage is of great interest specially in the processing of cryomilled powders which suffer from contamination as an unavoidable issue during their synthesis.

2.1.1. The electrical current

One of the particularities of SPS is the application of an electric field which, through Joule heat, provides the conditions of hot compaction. It results from this an enhancement of densification without microstructural change within a short processing time and a quality improvement (Olevsky E. A., 2007).

In SPS process, a pulsed sintering current of several kA passes into the sintering mold, and a part of the sintering current flows into the specimen whereas the other part flows pass through the die. The behaviour of the current flow depends strongly on the material being processed, be it conductive or non-conductive. Indeed, Misawa et al. (Misawa T., 2009) found the ratio of the internal current flowing through the specimen to the total current to be dependent on the material and the progress of SPS process. In other words, the amount, spatial distribution, and temporal behavior of internal current in the sintering body depend on the sintering stage and the electrical properties of the materials being processed as well as the die geometry and its physical properties. Locci et al. (Locci A.M., 2010), by performing simulations, found that the total current flowing through the specimen decreases with decreasing sample height, with increasing thickness of the spacers and with increasing diameter of the external die.

To study the effect of the current flow, Zadra et al. (Zadra M., 2007) inserted two alumina spacers between the graphite plungers and the powder to insulate the powder from the conductive punches and stop the current from passing through it, therefore allowing the current to only flow in the graphite die. They found improved

mechanical properties of the coarse aluminium when comparing this configuration to the case without alumina spacers .

Even though the absence of plasma is demonstrated (Hulbert D. M., 2009), the occurrence of occasional electric discharges is believed to take place on a microscopic level [Groza J. & Zavaliangos A. (2000). These phenomena contribute to the physical activation of the powder particle surface.

Wang et al. (Wang Y., 2002) studied the temperature distribution in the sample and in the die and found the difference directly related to the heat conductivity of the sample. However, in this modeling the authors did not include the graphite and the stainless steel spacers which definitely affect the current distribution. A more recent study was carried out by Anselmi-Tamburini and coworkers (Anselmi-Tamburini U., 2005) investigating by modeling and experimental observations the effect of current and temperature on two samples with a large difference in electrical conductivity, alumina and copper. Figure 2 shows the current distribution of both materials at room temperature applying a voltage of 4 V.

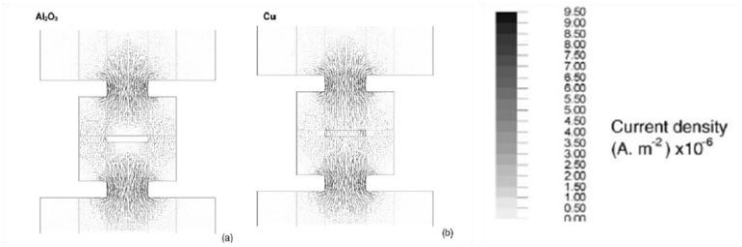

Figure 2: Current distributions in the SPS die for alumina and copper samples applying a voltage=5V (Anselmi-Tamburini U., 2005).

In this figure the current distribution passing through the sample is significantly different in both cases and the highest current densities are at the exposed parts of the plungers.

Very recently Guyot et al. (Guyot P., 2012) claimed the occurrence of the Branly effect at the early stages of the SPS process arising from the inductive effects generated by the pulsed current leading to the formation of melting in the contacting areas of particles.

2.1.2. The meaning of temperature in SPS

The temperature measurement during the SPS process is carried out inserting a pyrometer (or thermocouples) in a horizontal die hole about few mm from the loaded powders. Zavaliangos et al. (Zavaliangos A., 2004) analyzing the thermal gradients in SPS and using experimental measurements and finite element modeling, found the measured temperature much less than the actual one. They go against the quoted reduction in the sintering temperatures with respect to the conventional sintering techniques (HP, HIP) which they believe can be partially attributed to the lower measured temperature. Vanmeensel et al. (Vanmeensel K., 2005) stated that the thermal gradients inside the sample are mainly dependent on the presence of contact resistances between contacting parts and on the electrical properties of the specimen. They came to the conclusion that the best design is that consisting of focusing a pyrometer on the bottom of a borehole inside the upper punch about 5 mm away from the specimen centre inside the tool to measure temperature values much less dependent on both the presence of contact resistances and on the electrical properties of the specimen. More recently Tiwari et al. (Tiwari D., 2009) found out that the temperature difference between sample and die depends also on time of sintering and power input. Olevsky and Froyen (Olevski E., 2006) went through a further step and proposed a constitutive model based on grain boundary diffusion and power-law creep as the main consolidation mechanisms during SPS.

The high temperature attained at the particles' contact surface (Song X., 2006) and the subsequent melting (Guyot P., 2012) and soldering lead to the creation and increasing of electrical paths. This may lead to the formation of a finer microstructure as well a grain growth due to the non uniform distribution of temperature within the material during the sintering process.

2.1.3. The applied pressure

The primary role of pressure is believed to enhance sintering through particle re-arrangement (Munir Z. A., 2006). Its application enhances the densification mechanisms involved in free sintering through the increasing of vacancy gradient along grain boundaries leading to neck formation and growth while activating plastic deformation and grain-boundary sliding (Bernard-Granger G., 2009). This being strongly materials dependant on the nature and composition of the materials being processed.

It is worthy mentioning that the effect of pressure is strongly correlated to the densification stage. At the very first stage, the effective pressure is very high as the area over which the load is applied approaches zero (Anselmi-Tamburini U., 2013). It decreases proportionaly to a lower value at the final stage of densification.

The applied pressure is also dependant on the properties of the materials which define the temperature within it, and is correlated to the pores size and shape and gas pressure during the sintering process. In the case of amorphous materials, C.K. Kim et al. (Kim C. K., 2008) found out that highly densified and consolidated amorphous materials could be obtained in SPS without change in microstrcuture using high pressures. Consolidation of copper during SPS process has been the object of several other studies. Zhang et al. (Zhao-Hui Z., 2008) studied a copper particle size of 1 μm and obtained a 96% density using a holding pressure of 50 *MPa* at 750°*C*. An improvement of the densification was obtained in (Zhang Z. H., 2009) using an average particle size of 50 *nm* with a pressure of 600 MPa and a sintering temperature of 350°C for 5 min. This highlits the dependance of pressure on the particle size as this latter influences the thermodynamic driving force for sintering which is proportional to the specific surface area; it also influences the number and the extension of the contact areas and, in turn, the local pressure and electrical resistance which is of great importance in SPS due to the specific heating mechanism

It is worthy mentioning the importance of the temperature at which pressure has to be applied that and we have investigated it, ..

2.1.4. The heating rate

One of the significant advantage of SPS is the possibility of using high rates and thereby shortening the process which enables the sintering of nanopowders while keeping their microstructures unchanged. Kodash et al. (Kodash V.Y., 2004) investigated the effect on Ni nanopowders of heating rate varying it from 90 to 1100°C/min. They came to the conclusion that a moderate heating rate was beneficial to densification whereas a high one would lead a lower final density and a very high instead results in a nonuniform densification and the formation of cracks during sintering. Holland et al. (Holland T.B., 2010) claimed to successfully densify nanometric grain size of Ni combining fast heating rates and somewhat high uniaxial sintering pressures at low homologous temperatures which allows them to retain the low starting grain sizes with little to no grain growth. This enables obtaining bimodal distributions of nanometric and ultra-fine grains by by-passing the drawback effects of high stresses and non-equilibrium microstructures and achieve good mechanical properties. McWilliams et al. (McWilliams B., 2006) found instead that high heating rate can lead to a non-uniform density and compromised properties. Wang and coworkers (Wang Y., 2002) (Wang Y., 2002) outlined that the temperature difference between the sample and the die in SPS is directly related to heating rate and the sample's heat conductivity. According to Guo and coworkers (Guo Shu-Qi, 2008), the density of the sintered ceramics increases with increase in sintering temperature, heating rate, and holding time. However grain growth is favored by a low heating rate and longer holding time. Molinari et al. (Molinari A., 2012) investigated the effect of heating rate on the mechanical properties of spark plasma sintered nanostructured Fe-Mo powders. According to these authors, a high heating rate leads to some localized grain growth resulting in a broader distribution of grain size which is not the case for a low heating rate. It turns out from this a decrease of tensile strength and an increase of tensile ductility. At lower heating rate, the material behaves in a britle

way whereas at higher heating rate it undergoes plastic deformation with low strain hardening and tensile ductility up to 10%.

2.1.5. The holding time

Besides temperature, pressure and heating rate, holding time is a very important parameter as it may affect both the microstructure and density. Li et al. (Li B.R., 2003) found that increase in holding time, both grain size and density tend to increase. They also found that a holding time above 3 min flaken the grain which might be due to the uni-directional pressure which may force the grain to grow along some preferred orientation when the holding time increase. (Hungría T., 2009) found high holding time to be favoring grain growth. Investigating on the densification of Al_2O_3, Wang and coworkers (Wang S.W., 2000) claimed that lower holding time of 10 min led to microstructure inhomogeneity and found that a higher holding time of 30 min could a uniform density between the edge and the sample inside be obtained. Increasing the holding time from 5 to 30 min, Mouawad et al. (Mouawad B., 2012) improved the density of Molybdenum from 98,6 to 100 %.

2.2. SPS of nanostructured materials

Nanostructured materials have unique properties with respect to their micrometric scale counterparts. The high desire to preserve the advantages given by these materials when subjected to spark plasma sintering conditions has driven the attention of many researchers. Zhaohui et al. (Zhaohui Z, 2008) have studied the sintering mechanism of a large-scale ultrafine-grained copper during SPS. In analyzing the evolution of the microstructure, they clamed four stages (activation and refining of the powder, formation and growth of the sintering neck, rapid densification and plastic deformation densification) to be the prerequisite for a high quality bulk compact. They found a sintering temperature of 750°C, an initial pressure of 1 MPa, a holding pressure of 50 MPa, a heating rate of 80°C/min and a holding time of 6 min to be the optimized parameters for an improvement of the tensile strength and the

elongation of the ultrafine-grained copper. Using acryomilled 5083 Al alloy with an average crystallite size of about 25 nm and consolidating with SPS at 350°C, 80 MPa and 300 s, Ye et al. (Ye J., 2006) obtained a fully dense bulk material with a bimodal grain size distribution of about 47 and 300 nm. Through the study of the microstructure and densification rate, they came to the conclusion that plastic yielding, viscous flow, creep and diffusion are the involved mechanisms of densification. They found the nonuniform current flow within the material being effecting the mass transport phenomena and highly affecting size distribution as well as creep and diffusion rates.

The influence of the SPS process on the microstructure, aging response and mechanical properties of a cryomilled Al-Cu-Mg-Fe-Ni-Sc alloy was examined by Zúñiga and coworkers (Zúñiga A., 2006), the first report on the consolidation of cryomilled Al powders by SPS. In their work, they reported the production of a bimodal aluminum grain structure with a dispersion of Al_9FeNi, Al_2CuMg and Si-rich particles in the matrix. They claimed the coarse-grained regions being the result of the generation of high current densities at the particles' contact zones during the first stages of the sintering process. To explain the lack of precipitation of rodlike S' Al2CuMg, they put forward the possibility for nanometric grains to provide a kinetic constraint to precipitation reactions and relate the high thermal stability of the alloy to solute drag and Zener pinning caused by impurities introduced during milling process. Very recently Wen and coworkers (Wen H., 2011) examine the influence of oxygen and nitrogen contamination on the densification of cryomilled copper powders during SPS. They found the difficulty to obtain full density related to the thermal decomposition of O and N based compounds to gaseous species which lead to porosity formation. It turns out that the cryomilled material should undergo thermal annealing before in order to improve the densification process.

2.2.1. Improvement of the mechanical properties by bimodal size distribution.

In this section the production of bimodal distribution to overcome the low ductility of nanostructured materials as a result of the small grain size will be reviewed. A limited dislocation activity and the subsequent absence (or poor) work hardening cause nanostructured metallic materials to exhibit a significantly high strength at the expense a low ductility resulting in a low fracture toughness which limit their pratical use (Siegel R.W., 1995; Koch C.C., 1999; Mukherjee, 2002; Kumar K.S., 2003; Wolf D., 2005; Dao M., 2007 ; Koch, 2007; Ovid'ko, 2007), since tensile ductility is controlled by a competition between plastic deformation and fracture processes as well as by the resistance to plastic flow localization (Figure 3) (Ovid'ko I.A., 2012). Instead of experiencing a homogeneous plastic deformation (Figure 3b), in NC metals with a grain size lying within 10-30 nm, a brittle crack nucleation and propagation instabilities (Figure 3c) are the main process which responsible for low ductilities. Moreover, in the case of NC metals with high grain sizes up to 100 nm and ultrafine-grained (UFG) ones (100-1000 nm), plastic strain instability is the process which lower ductility.

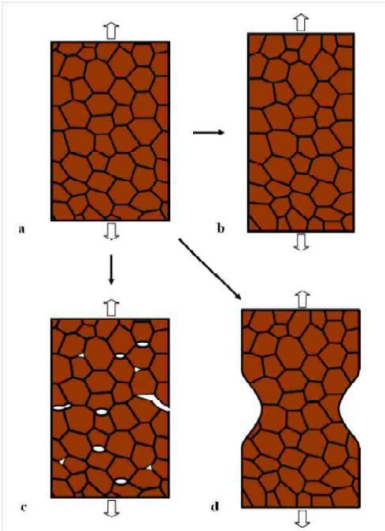

Figure 3: Evolution routes of a nanocrystalline (NC) specimen under tensile load. (a) Initial state of the NC specimen. (b) Homogeneous plastic deformation of the specimen corresponding to its enhanced ductility. (c) Brittle fracture in the NC specimen occurs through crack nucleation and growth instabilities, typically involving the fast nucleation of nanoscale cracks, their convergence and/or growth along the grain boundaries. (d)The specimen shows plastic strain instability with necking. Routes (c) and (d) correspond to low tensile ductilities (Ovid'ko I.A., 2012).

It is worthy mentioning that the low ductility, instead of being intrinsically related the nanocrystalline and ultrafine-grained metals, may be arising from the extreme flaws such as porosity, poor interparticle bonding (Figure 4), impurities and the high internal stresses that take place during the processing stage of the nanocrystalline materials which lead to premature failure in tensile deformation (Sanders P.G., 1997; Sanders P.G., 1997).

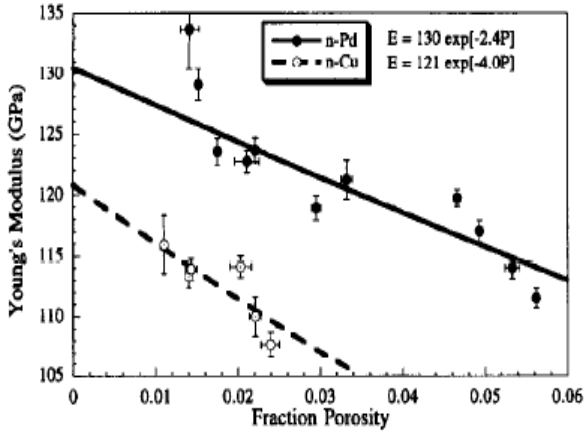

Figure 4: Young's Modulus as a funtion of porosity for nanocrystalline Cu and Pd (Sanders P.G., 1997).

In order to enhance ductility wile keeping the high strength, the aforementioned instabilties must be suppressed. A modification of the microstructure in the nc and UFG regime is therefore necessary to attain high levels of strength and ductility (Wang Y. M., 2002). One way of doing so is to produce a single-phase bulk material with bimodal structures, embedding large grains within the nanometric and ultrafine grains matrix (Wang Y., 2002; Wang Y.M., 2004; Sergueeva A.V., 2004). The presence of large grains is believed to suppress crack propagation and provide strain hardening which is responsible for the ductility improvement: The nanometric grains instead, account for a high strength and high hardness (Ovid'ko I.A., 2012).. By incorporating larger grains in a fine-grained matrix (Legros M, 2000; Tellkamp V. L., 2001), the authors achieved an improvement of strength and ductility of both Cu and Al 5083. They obtained 535 MPa and 334 MPa and 2,1 and 8,4 % for strength and elongation, respectively.

Grain growth (Tellkamp V. L., 2001) or recrystallization (Legros M, 2000) are possible ways through which large grains may forme within the fine-grained structure. In the first case,

In their investigation on the consolidation of copper powder with an average size of 50 nm, Zhang et al. (Zhang Z. H., 2009) found temperature significantly affecting density and yield strength, and reported the former to be defining the latter. The authors claimed the production of highly dense (> 99 %) nanocrystalline bulk copper with a Yield Strength of about 650 MPa be possible using a sintering temperature of 350°C at a heating rate of 100°C/min, a holding pressure of 600 MPa and a holding time of 5 min.

Chapter III

Experimental procedure

3.1. The atomized copper powder

In the present PhD work, a commercial water atomized copper powder produced by Pometon Powder, Metal Powders and Granules with a purity of 99,6 % and a particle size < 100 μm was used. The material contained 0,2 % of oxygen.

3.2. Cryomilling

There are several advantages to cryomilling as compared to milling at room temperature. First, powder agglomeration and welding to the milling media are suppressed, resulting in a more efficient milling outcome (e.g., improved yield and structure refinement). Second, oxidation reactions during milling are reduced under the protection of a nitrogen environment. Third, the milling time required to attain a nanostructure is significantly reduced, because the low temperature suppresses the annihilation of dislocations and the accumulation of a higher dislocation density is possible (Lavernia E.J., 2008)

In this PhD work, a modified Union Process 01-HD attritor was used to produce nanostructured copper powders. The powder was cryomilled in a liquid nitrogen medium without any Process Control Agent (PCA). INOX AISI 440-C spheres of 6 mm in diameter were used as the griding media with a ball to powder mass ratio (BPR) of 30:1. Milling was performed at 300 rpm for 8h.

After cryomilling, the milled powder was transferred in a glove box where the nitrogen was allowed to evaporate under a controlled atmosphere to avoid contamination and oxidation.

The sieving process was performed using a stack of three sieves of 25, 45 and 90 μm in a decreasing mesh size.

The cryomilled copper after sieving into two granulometric ranges (< 25 and 25 – 45 μm) underwent thermal analysis via Differential Scanning Calorimetry (DSC) and Thermogravimetry (TG) under argon atmosphere. A DSC7 Perkin Elmer apparatus was used to perform DSC on the cryomilled powder at a flow rate of 20 ml/min and at different heating rates (15, 20,30°C/min). An alumina (Al_2O_3) pan was used as a sample holder and measurements were performed from room temperature to 600°C with a cooling rate of 50°C/min. The cryomilled powder was scanned twice to get the reference line to substract the instrumental thermal effect.

Thermogravimetry Analysis (TGA) analysis was carried out on a Netzsch STA 409 PC/PG apparatus at a heating rate of 10°C/min and scanning was performed twice from room temperature up to 900°C.

The powder underwent also heat treatment using a Tersid tubular high vacuum furnace (10^{-5} mbar) at different temperatures (290, 300, 400, 500 and 600°C) for two hours (2h) of isothermal holding.

Nitrogen and oxygen analyses were carried out using LECO TC400 machine®.

3.3. Spark Plasma Sintering

SPS was carried out using a SPS-1050 machine (Sumitomo Coal & Mining Co. Ltd) with pulsed DC voltage (pulse cycle: 12 pulses ON/2 pulses OFF, duration 3 ms). Disks of 10 and 20 mm diameter and 5 mm height were produced using graphite die and punches. An initial pressure of 6 and 25 MPa was applied at the beginning of the SPS cycle. In most of the cycles, a final pressure was then applied at different temperatures, up to 60 MPa. Temperature during SPS cycles was monitored by a thermocouple inserted in a blind hole in the die wall, at a distance from the internall surface of 1 mm. Since the actual tempeperature in the powder is different from that measured in the die, the monitored temperature has to be considered as a nominal one and is smaller than the actual one.

3.4. Characterization procedures

The density (ρ) of the sintered specimens was measured with the Archimedes method according to ASTM B962-08 using the following equation:

$$\rho = \frac{M}{M - M_a} \rho_{water} \qquad (1)$$

where M is the mass of the SPS sintered specimen and M_a its apparent mass under water and ρ_{water} the density of distilled water at the measurement temperature. M and M_a were obtained using an AdventurerSL OHAUS balance with a precision of 0.0001g.

Metallographic preparation of the obtained discs was made through grinding using abrasive papers of 220, 500, 800, 1200 and 4000 grits followed by polishing using a 3μ and 1μ slurry on a diamond pad using a OP-S suspension. In order to analyse the microstructure, the metallographic specimens were etched using a solution of 35 ml of nitric acid in 100 ml of distilled water for a few seconds.

A Zeiss Light Optical Microscope was used for microstructural characterization and the acquirement of the images was obtained through a Leica DC300 software.

Scanning Electron Microscope (SEM) was carried out on a Philips XL30 apparatus for the observation of powder morphology, microstructural details of both powder and sintered materials and fracture surface of the latter ones.

X-ray Diffraction (XRD) characterization was performed using Mo Kα (λ = 0.71069 nm) radiation at 40 kV and 40 mA and a scan rate of 0,02 deg/s. The instrumental contribution to the line profile was determined from a measurement of the NIST LaB6 line-profile standard (SRM 660a). Quantitative analysis (QA) of the copper oxide phase which was used to calculate the theoretical density (ρ_{th}) of the cryomilled material was obtained using MAUD (Materials Analysis Using Diffraction) software (Lutterotti L., 1997). Structural characterization (crystallite size and dislocation density (ρ_{disl})) was performed using PM2K (Leoni M., 2006) software. TEM studies were conducted on a Philips CM12 microscope operating at 120 kV as a combine technique with XRD. TEM foils were cut from sintered materials and mechanically

ground to a thickness of less 100 µm prior to an extra thinning with a 6 kV Ar^+ ions milling up to a thickness of about 30 nm.

Microhardness (µHV) measurement of the polished disks was carried out using a Vickers indentation *MHT*-4 hardness testing device. The applied load was 0,5 *N* and the loading time 10 *s*. The test was always performed 10 times to have a better representativity and around the middle of the specimen to avoid near-surface effects.

Mechanical characteristics of the SPSed cryomilled copper were studied by means of tensile tests using an Instron 8516 SH device. Tensile test pieces of ~4,9 x 4,9 mm^2 cross section and a gauge length of 12,50 mm length (ASTM E8M-04 or ASTM E8M-04) were then produced and tests were carried out with a strain rate of 0,1 s^{-1}.

Chapter IV

Results and discussion

4.1. The atomized copper powder

4.1.1. A DOE study of the effect of temperature, pressure and particle size

Two granulometry classes (<25 and 25–45 µm) were used by to study the effects on the SPS densification process of three factors: X_1, X_2, X_3 corresponding to particle size, sintering temperature and pressure respectively, as well as the interaction effects. Discs with 20 mm diameter and 5 mm height were produced. A full 2^3 factorial design without replication was implemented**.** The three factors are varied at two levels **(**Table 1**)** and the number of experiments was eight **(**Table 2**)**.

Table 1: Factor settings for the DOE investigation of SPS process

Code	Factor	Unit	Low (-)	High (+)
X_1	Particle size	µm	< 25	25 – 45
X_2	Temperature	°C	600	700
X_3	Pressure	MPa	20	30

The temperature and pressure levels were defined after preliminary experiments which shown that a full density can be obtained at 800°C and 40 MPa on both the particle sizes. Both factors were then settled to lower values (600 and 700°C, and 20 and 30 MPa, respectively) to obtain density results in a range wide enough to allow the effect of the factors to be highlighted. Pressure was applied in two steps in all the experiments: the initial pressure of 6 MPa (to establish the electrical contact between punches and particles) was increased up to the final value when temperature

reached 500°C. The relative density obtained with reference to the theoretical one (8.92 g/cm^3) is shown in Table 2.

Table 2: 2^3 factorial design matrix and density of spark plasma sintered copper

Test	Particle size	Temperature	Pressure	Density/%
1	-	-	-	69.4
2	+	-	-	84.2
3	-	+	-	89.9
4	+	+	-	92.8
5	-	-	+	77.7
6	+	-	+	84.6
7	-	+	+	93.8
8	+	+	+	92.8

Data were analyzed using R software (Team, 2010). Equation (2) is the empirical formula describing the effect on density of each parameter as well as the interaction effects between them

$$\rho = \alpha_0 + \alpha_1 \overline{X_1} + \alpha_2 \overline{X_2} + \alpha_3 \overline{X_3} + \alpha_{12} \overline{X_1 X_2} + \alpha_{13} \overline{X_1 X_3} + \alpha_{23} \overline{X_2 X_3} + \alpha_{123} \overline{X_1 X_2 X_3} \qquad (2)$$

Where $\overline{X_1}$, $\overline{X_2}$ and $\overline{X_3}$ are the factors effecting on the response ρ representing density of the spark plasma sintered copper. α_0, α_1…represent the factorial effects.

ANOVA is used to assess the significance of the effects on densification mechanism from the SPS parameters. In the ANOVA model the density given by equation (2) is assumed to be the result of the added effects of particle size, temperature and pressure as well as their interaction.

The results of ANOVA are reported in Table 3 where the sum of squares and mean squares for the main and interaction effects are given.

Table 3: ANOVA table with parameters effects

Source of variation	Df	Sum of squares	Mean squares	F value	Pr (>F)
X1	1	69.62	69.62	34.8100	0.1069
X2	1	356.44	356.44	178.2225	0.0476*
X3	1	19.84	19.84	9.9225	0.1957
X1X2	1	49.00	49.00	24.5025	0.1269
X1X3	1	17.40	17.40	8.7025	0.2081
X2X3	1	2.88	2.88	1.4400	0.4423
Residuals	1	2.0	2.0	……	…..

F-test, which is used to compute the variance ratio, gives the significance of each factor. The Pr values which are compared to a significance level of 0.05 are also evaluated. Indeed, the smaller the Pr value with respect to 0.05, the higher the effect of its corresponding factor. The lowest value of Pr corresponding to temperature indicates temperature as the main SPS parameter influencing density. This is illustrated in Fig. 5a. In this figure it can be observed a linear relationship between the factors theoretical quantiles which validate the linear model assumptions of normality. All the points that fall close to the reference line provide an indication of univariate normality of the dataset. However, the high deviation of factor X_2 (temperature) from the straight line explains its highest impact on the densification mechanism. In order to gain more information, Fig. 5b compares the factors main effects. Indeed, in this figure the length of each segment is indicative of how much is the change in density when the corresponding parameter is changed from a low to a high level. This allows us to confirm the temperature as the most effecting parameter on density followed by particle size and then by pressure.

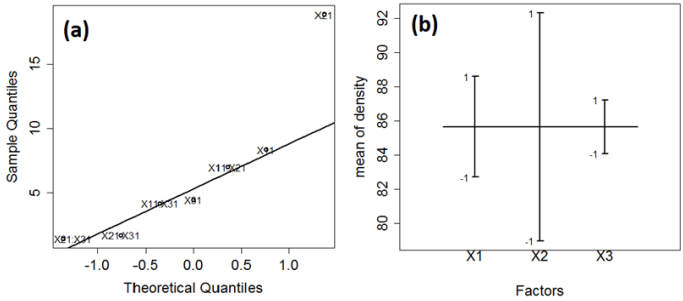

Figure 5: (a) normal Q–Q and (b) model design plots of factors effects on density

The correlation between the SPS process controlling parameters and the density of the produced specimens is given by equation (3)

$$\rho = 85.650 + 2.950\overline{X_1} + 6.675\overline{X_2} + 1.575\overline{X_3} - 2.475\overline{X_1X_2} - 1.475\overline{X_1X_3} - 0.600\overline{X_2X_3} \quad (3)$$

The testing of the validity of the model can be conducted applying equation (3) to the experimental conditions in Table 2. Table 4 shows the deviation D (%) between the experimental density ρ_{ex} and the predicted one ρ_p from the model design, calculated with equation (4)

$$D = \frac{\rho_p - \rho_{ex}}{\rho_p} \times 100 \quad (4)$$

Table 4: Deviation D between experimental density ρ_{ex} and predicted density ρ_p

Test	ρ_{ex} (%)	ρ_p (%)	D (%)
1	69.4	69.9	0.7
2	84.2	83.7	-0.6
3	89.9	89.4	-0.6
4	92.8	93.3	0.5
5	77.7	77.2	-0.6
6	84.6	85.1	0.6
7	93.8	94.3	0.5
8	92.8	92.3	-0.5

The low values of D confirm the high matching of the model with the experimental data.

The interaction effects obtained between the different parameters from DOE analysis using R are shown in Fig. 6.

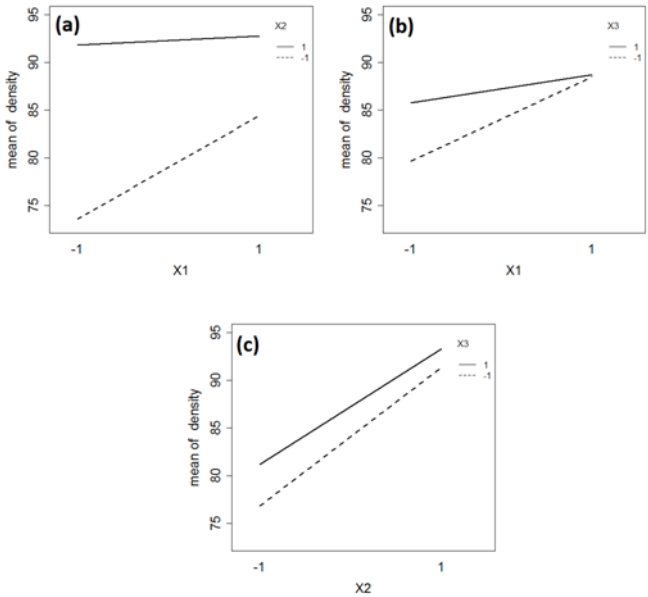

Figure 6: (a) particle size–temperature, (b) particle size–pressure and (c) temperature-pressure interaction effects on density

It can be seen that the effect of a parameter depends on the levels considered and that density performs better at high levels (coarse particle size, high T and high P). The interaction plot of particle size and temperature on density (Fig. 6a) shows a synergic interaction effect. It can be seen that at any particle size level, density performs better at a high temperature level. It can be also seen that, despite of the

larger driving force for sintering, density performs better at a high particle size level. The increasing temperature is more effective on the fine powder than the coarse one. The fine powder results in better resistance to densification than the coarse one despite of the larger thermodynamics force.The effect of particle size and pressure (Fig. 6b) shows a synergic interaction. At a low particle size level, density performs better at a high pressure level. However, at a high particle size level, the change in pressure does not affect density. Finally, Fig. 6c shows that there is a very slight interaction between pressure and temperature and therefore, the important effects are the main ones. At any temperature level, density performs better at high pressure, but the effect of an increasing pressure on density is high at low temperatures since particles are less deformable. A high temperature softens the materials that become easily deformable and the effect of increasing pressure is less pronounced.

The punch displacement versus temperature curves are shown in Fig. 7 to describe the progress of densification process as temperature increases for the different combinations.

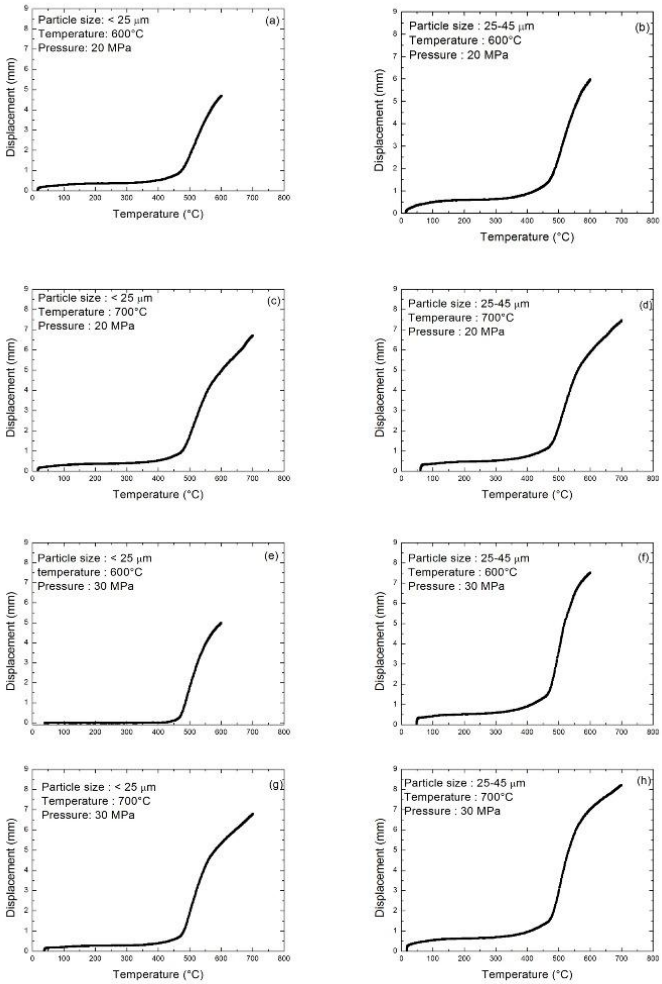

Figure 7: Displacement versus temperature curves of SPS experiments

Within the same particle size and keeping the pressure constant (Figures 7a–c, e–g, b–d and f–h), densification improves with increasing temperature, in particular in a finer particle size. Moreover, keeping the temperature at 600°C, densification

increases with pressure (Figures 7a–e and b–f) in particular in the coarser particle size. At 700°C, no improvement is observed in the finer particle size (Fig. 7c–g), whereas in the coarse particle size (Fig. 7d–h) densification performs better with increasing pressure. Keeping temperature and pressure constant, densification increases with particle size (Figures 7a–b, c–d, e–f and g–h).

The SEM fractographs of the specimens are shown in Fig. 8.

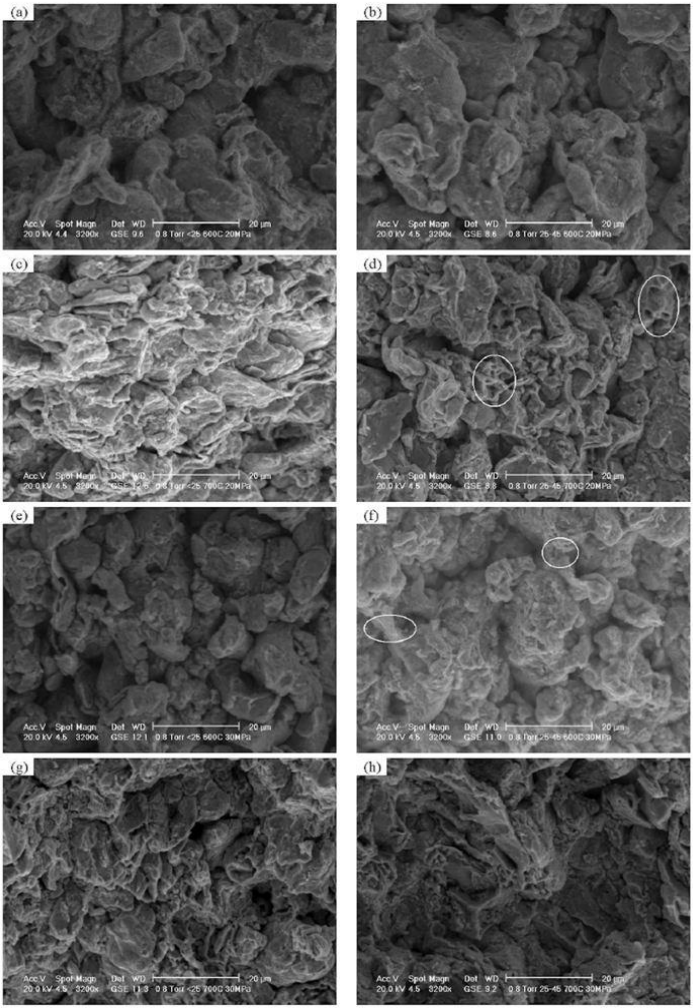

Figure 8: SEM micrographs for fracture surface of the Spark Plasma Sintered copper. (a) <25 μm , 600°C, 20 MPa; (b) 25-45 μm, 600°C, 20 MPa; (c) <25 μm, 700°C, 20 MPa; (d) 25-45 μm, 700°C, 20 MPa; (e) < 25 μm, 600°C, 30 MPa; (f) 25-45 μm, 600°C, 30 MPa; (g) < 25 μm, 700°C, 30MPa and (h) 25-45 μm, 700°C, 30 MPa

In Fig. 8a and b as well as in Fig. 8e and f (low temperature), the shape of the starting powder can still be recognized and particles are only slightly deformed in Fig. 8b and f (coarse particles). Some necks are visible in Fig. 9f (high pressure and coarse particles). The increase in temperature (Fig. 8c, d, g and h) up to its high level leads to particle deformation. In these pictures, the shape of the starting particles cannot yet be recognized due to enhanced deformation. Necks are visible and dimples (significant for a metallic bonding in the necks) are present in coarse particles in Fig. 8d and h only.

The differences in morphology between Figures 8a, b, e, f and Figures 8c, d, g, h, corresponding to an increase in temperature, are more relevant than those between Figures 8a, b, c, d and Figures 8e, f, g, h which correspond to an increase in pressure. This is due to the fact that at 700°C the material is heated enough to be easily deformed resulting in densification and consolidation. This phenomenon is enhanced in the coarse particle.

The main results of the present investigation may be summarized as follows. In the temperature and pressure ranges investigated densification is mainly due to deformation, and neck formation and growth (recognizable by the dimpled morphology on the fracture surface) occur only at a high temperature and pressure and in particular in the specimens produced with the coarse particles. The fine particles result in higher resistance to densification (to deformation) than the coarse ones. ANOVA indicates that temperature has the main effect on density, followed by particle size and by their interaction. The effect of pressure and of its interaction with particle size and even more with temperature are the less pronounced.

The particle size influences the number of particles in the compaction section and, in turn, the local value of the force applied to the contacts points, the extension of the contact area, the actual pressure and the electrical resistance. This last parameter influences the current flow and, in turn, the local temperature (due to Joule effect) and the field assisted mass transport phenomena since it changes the defect concentration and enhances their mobility (Munir Z. A., 2006) **.** In a simplified approach, a cubic arrangement of spherical particles with two diameters: 16 and 32 mm as representative of the two particle size classes here investigated, is assumed

to represent the powder during SPS. The number of contact points in the compaction section is in the ratio 4 (16 mm) : 1 (32 mm). This means that the actual normal force FN applied is four times higher on the larger particle than on the fine one. In a first approximation, the radius of the contact area a may be calculated by applying the theory of the elastic contact (Johnson, 1985) from equation (5) valid for the contact between spheres

$$a = \left(\frac{3F_N R'}{4E'} \right)^{1/3} \qquad (5)$$

where F_N is the normal force on the single particle (given by the ratio between the applied force F= 2 kN and the number of particles in the compaction section), R' and E' are the equivalent radius of curvature and the equivalent elastic modulus respectively. They are given by equations (6) and (7)

$$\frac{1}{R'} = \frac{1}{R_1} + \frac{1}{R_2} \qquad (6)$$

$$\frac{1}{E'} = \frac{1-\nu_1^2}{E_1} + \frac{1-\nu_2^2}{E_2} \qquad (7)$$

where R_1 and R_2 are the radius of particles 1 and 2 and E_1, ν_1, E_2 and ν_2 are their corresponding elastic modulus and Poisson's ratio, respectively. The elastic constants of copper are $E_1 = E_2 = 105 \times 10^9$ Pa and $\nu_1 = \nu_2 = 0.30$. The radius of the contact area in the case of the two particles sizes considered results in the ratio 1 : 2.

The radius of the contact area influences the pressure applied to the single particle to particle contact and the electrical resistance. The pressure can be represented by the maximum Hertzian pressure P_{max}, given by equation (8)

$$P_{\max} = \frac{3F_N}{2\pi a^2} \qquad (8)$$

and results in the ratio 1 : 1.02 for the two particle sizes above considered. The local pressure results almost independent on the particle size, being only 2% higher on the large particles. The electrical resistance R at the contact between particles decreases with the extension of the contact area S according to equation (9)

$$R = \frac{\rho h}{S} \qquad (9)$$

where ρ is the electrical resistivity of copper and h is the thickness of particle. The extension of the contact area is in the ratio 1 : 4 for the two particle sizes considered. Therefore, the electrical resistance decreases significantly with the particles size and as a consequence, the current density and, in turn, temperature increase. Song et al. (Song X., 2006) calculated the temperature profile along the radius of a spherical particle using equation (10), demonstrating that an extremely large superheating occurs on the surface of the particles, capable to melt and evaporate the surface layers

$$\Delta T = \frac{16}{\pi^2} \frac{I_p^2 \rho \Delta t}{C_v \rho_m} \left[\frac{1}{r^2 - (r-x)^2} \right]^2 \qquad (10)$$

$$I_p = \frac{4r^2}{\phi^2} I_S \qquad (11)$$

where ρ = 1.67 x 10^{-3} Ω.cm, ρ_m = 8.92 g.cm^{-3}, C_v = 24.44 J.K.mol^{-1}, Φ = 20 mm (the inner diameter of the die which is the same as the sample diameter), I_S = 1000 A and Δt = 12 x 0.0033 $\approx$ 0.04 s. The temperature profile in the two particles sizes here considered was calculated for a nominal temperature of 500°C, and the results are shown in Fig. 9.

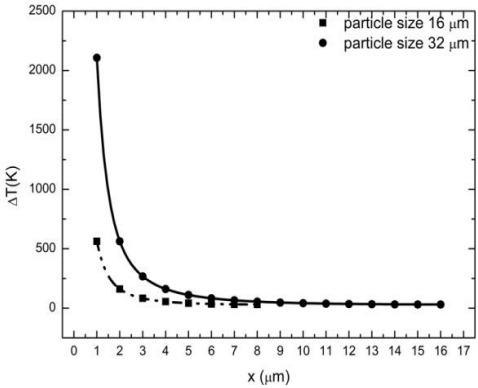

Figure 9: Distribution of temperature increase in particle from surface to core

The large overheating of the surface layers is confirmed and the temperature profile decreases sharply on moving towards the particle center. The temperature reached on the surface of the coarser particle is significantly higher than that on the finer one. Consequently, localized melting, thermal softening of the subsurface layers and field activated mass transport phenomenon in the contact regions are enhanced. The effect of particle size on densification is therefore due to the influence of the local current flow. It activates melting in the contact points and the field assisted mass transport phenomenon on one side and thermal softening on the other one in the underlying layers. This justifies the effect of the interaction between temperature and particle size highlighted by ANOVA. The effect of pressure is minor since pressure does not contribute to melting in the contact points and the resistance to plastic deformation of the underlying layers is quite low.

Only two classes of particle size were investigated in the present work based on a full factorial 2^3 DOE approach. Nevertheless the positive effect of the particle size on densification in the temperature and pressure ranges here considered was confirmed by carrying out SPS experiments on a 45–90 μm powder. A further enhancement of

the densification process was observed. The local pressure on a 64 μm particle, taken as representative of this granulometry class, is only 3% larger than that on a 16 μm particle, confirming the poor effect on actual stress promoting deformation. On the other hand, the surface overheating is much higher than on the smaller particles, confirming the large effect on the melting and thermal softening which assist neck formation and deformation.

4.1.2. The densification and sintering mechanisms

The atomized copper powder was sieved in three particles size ranges (< 25, 25 – 45 and 45 – 90 μm) and used for the production of disks of 10 mm diameter and 5 mm height. A pressure P_i = 25 MPa was applied at the beginning of the SPS cycle; this is the minimum pressure applicable, corresponding to the minimum force which has to be applied to establish proper electrical contacts between powders and punches corresponding to a specimen disk of 10 mm. Pressure was then increase up to P_f = 60 MPa, at different temperatures in the different experiments. Heating rate was 100 °C/min and the isothermal holding time at the sintering temperature was 2 min.

The relative density was calculated with reference to the theoretical one (ρ_{th}) of 8,920 g/cm^3.

Fig. 10 shows the displacement rate vs. temperature curve of the 25 – 45 μm powder sintered with the initial pressure P_i.

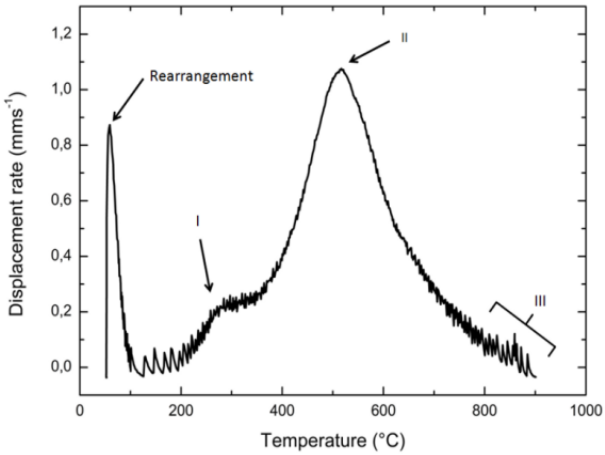

Figure 10: SPS displacement rate curve

The displacement rate shows three peaks: a sharp peak at low temperature, a weak peak at 270-290°C and a broad peak with the maximum displacement rate at 517°C. The first peak can be attributed to the initial rearrangement of the powder particles due to P_i. To interpret the second and third peak, SPS experiments were carried out up to 450, 600 and 900°C and specimens were broken to observe the fracture surfaces, which are reported in Figure 11.

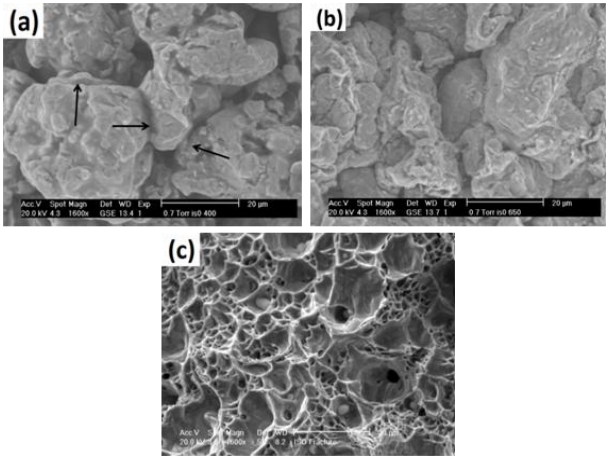

Figure 11: Fracture surface of the sintered specimens up to a) 400°C, b) 650°C and c) 900°C

The fracture surface of the specimen sintered at 400°C (Fig. 11a) shows only a few necks (indicated by arrows) and no decohesion zones with by the typical dimpled fracture morphology of copper. Particles are slightly deformed at the surface (localized deformation). At 650°C (Fig.11b), an increased packing along with an increased deformation of the particles can be observed. Deformation is no more localized at the contact zones but still no dimples are observed. The fracture morphology clearly indicates that most of the particles are increasingly packed but not yet sintered at the two temperatures. This observation agrees with the results presented by Song et al. (Song X., 2006), where a dimpled fracture is not observed until 770°C in a fine spherical powder processed under similar conditions as in the present work. The two displacement rate peaks shown in Figure 12 are therefore due to the plastic deformation of the powder particles, which involves the contact areas at the lower temperature and propagates in the core at the high one. The intensity of the two peaks and the extent of densification involved are then correlated

to the intensity of deformation: a localized deformation results in a slight densification, whilst the propagation of deformation in the core promotes a large densification. Temperature enhances deformation.

The observation of only a few necks and the absence of a ductile fracture morphology indicate that sintering phenomena responsible for the formation of metallic bonding between particles, did not occur up to 650°C, even if density has increased significantly. In other words, the material is densified, but not yet sintered.

The fracture surface of the specimen sintered at 900°C (Fig. 11c) shows a fully dimpled fracture indicative of an effective consolidation of the material . The original particles cannot be yet recognized. It may be concluded that mass transport phenomena responsible for neck formation and growth mainly occur between 650°C and 900°C. The displacement rate in this temperature range decreases continuously since powders have been already densified by deformation, and therefore the effect on densification rate is small.

The three peaks of the displacement rate curve can be therefore attributed to the following phenomena: rearrangement, localized deformation at the contact points, core deformation. Extensive sintering by mass transport phenomena occurs in the last part of the SPS cycle (Fig. 12).

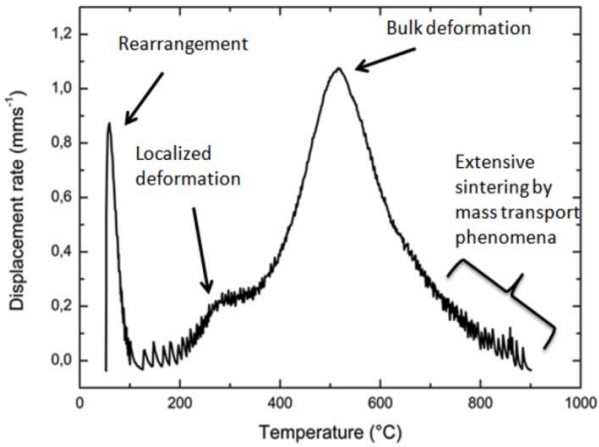

Figure 12: Displacement rate versus temperature

Fig. 13 shows the displacement and displacement rate vs. temperature of the three different particles sizes (< 25, 25-45 and 45-90 μm) when sintered under the initial pressure P_i.

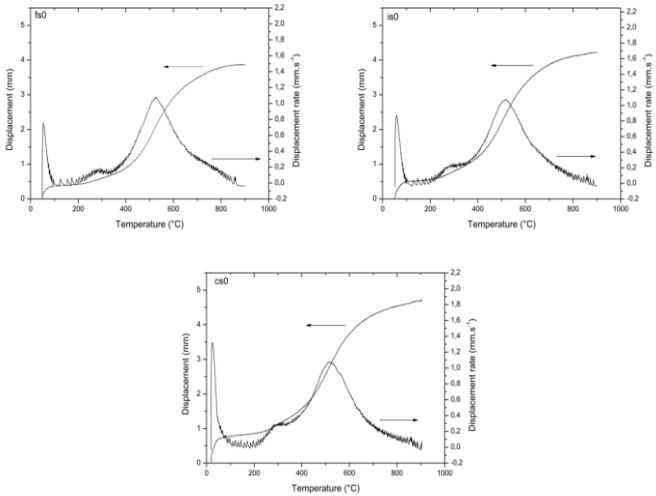

Figure 13: Displacement and displacement rate versus temperature of the three different particle size applying only the initial pressure

The height of the rearrangement peak increases with particle size. Rearrangement occurs through the relative movement of the particles and is opposed by the interparticle friction at the contact points. Since the number of contact points per unit volume decreases on increasing particle size, rearrangement is enhanced by large particles, as actually observed.

On increasing particle size both the height and the width of the localized deformation peak is increased whilst the bulk deformation peak does not change significantly. This means that the increase in particle size enhances the localized deformation but not the bulk deformation. To interpret this effect, the influence of the particle size on the local pressure and on the local overheating at the particle contacts is analyzed.

The local pressure is the pressure applied to a single particle contact and, in a first approximation, may be calculated with the theory of the elastic contact assuming a

spherical particle shape . Using Equations (5), (6), (7) and (8), the maximum hertzian pressure P_{max} can be calculated, given an applied force of F_N = 2 kN.

Assuming a simple cubic arrangement of spherical particles and three diameters: 16, 32 and 64 μm as representative of the three particle size classes here investigated, the normal force F_N is in the ratio 1:4.2:17.3, the radius of the contact area in the ratio 1:4:16 and the local pressure in the ratio 1:1.02:1.03 The influence of particle size on the local pressure is almost negligible.

With reference to the three particle sizes above considered, 16, 32 and 64 μm, the contact area is in the ratio 1:4:16. The decrease of the resistance, given by Equation (9), with particles size increases the current flow and, in turns, temperature at the contact regions. The peculiar heating system of SPS promotes a large overheating at the particle contacts, which can be calculated with the model proposed by Song et al. (Song X., 2006) from Equation (10). Overheating for the three particle sizes at four different temperatures is shown in Figure 14.

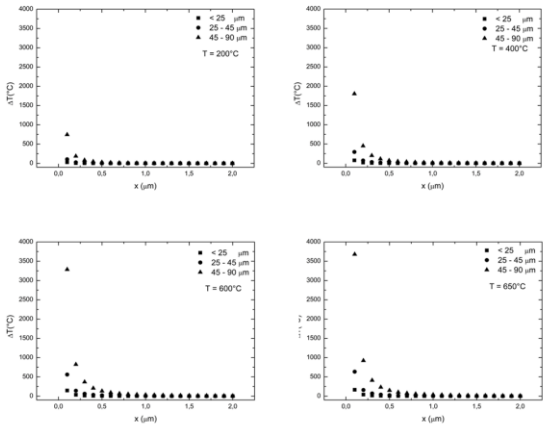

Figure 14: Temperature increase profile from surface to the core of particles

The temperature increase at the surface of particles is very pronounced and raises on increasing particle size. Overheating involves a very thin surface layer: as an

example, ΔT in the coarse powder at the SPS temperature of 650°C is 920°C at 0.2 μm, 150°C at 0.5 μm, 76°C at 0.7 μm and 2°C at 1 μm. Such a localized overheating causes thermal softening and localized melting at the surface, both enhancing deformation and promoting the formation of necks (even by melting and re-solidification). On increasing particle size the local overheating increases dramatically; local thermal softening and melting support densification and formation of sintering necks. This justifies the enhancement of the localized deformation with particle size. On the other side overheating does not affect the particle bulk temperature and, in turn, bulk deformation; therefore the corresponding displacement rate peak does not change on increasing particle size.

Despite of the positive effect of particle size on overheating and deformation, the final density slightly decreases with particle size: 100%, 98,6% and 97,8% of theoretical density for fine, intermediate and coarse powder, respectively. As a confirmation, the displacement curve reported in Figure 13 is flat (no densification) at 900°C only for the fine particle size, whilst it is still increasing (active densification) for the intermediate and, slightly more, for the coarse particle size. The mass transport phenomena responsible for sintering in a micrometric powder is power law creep, (Olevsky E., 2006) whose effect on shrinkage increases on decreasing grain size. This dependence accounts for the different sintered density of the three specimens.

Figure 15 shows the microstructure of the three sintered specimens. The grain size increases with particle size.

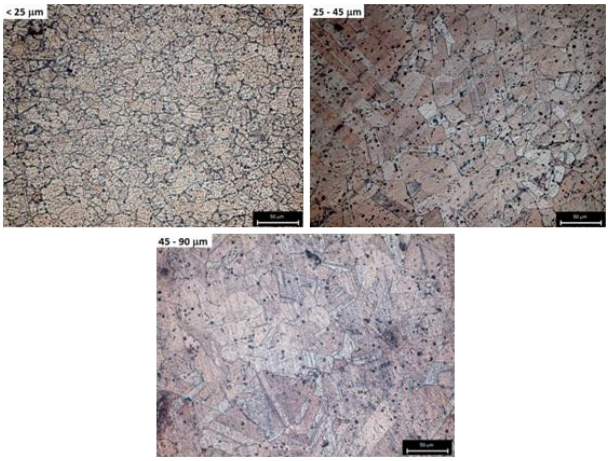

Figure 15: Microstructure of the sintered specimens applying only the initial pressure

In sintering porosity limits grain growth because of the pinning effect exerted by pores. This occurs in SPS, too, as reported by H. Z. Zhang et al. (Zhang Z. H., 2008) for ultra-fine copper. Even if density differences are quite small, the larger grain size is shown by the less dense material. The justification for this apparent contradiction can be found in the effect of the size of the powder particle (which is a polycrystalline aggregate) on its grain size: the coarser the particle, the larger grain size. Therefore, the sintered specimens keep memory of the grain size of the starting powder.

To increase density of the specimens produced with the intermediate and the coarse powder, pressure was increased during the SPS cycle at three different temperatures:

-) 300°C, i.e. during the localized deformation step;

-) 600°C, i.e. after the bulk deformation step;

-) 900°C, i.e. at the end of the heating step.

Figure 16 shows the displacement and displacement rate versus temperature for the intermediate particle size.

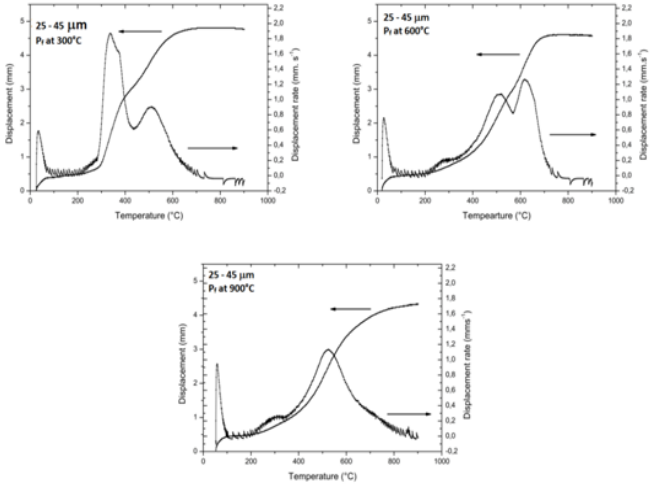

Figure 16: Displacement and displacement rate versus temperature of the 25-45 µm powder sintered applying pressure at 300, 600 and 900°C

At 300°C, the application of P_f causes a sharp densification rate peak but, despite of the large densification promoted, the bulk deformation peak is still present, with a slightly lower intensity than that of the previous experiments without P_f (figure 13). The poor effectiveness of this "early" application of pressure is demonstrated by the fracture surface of a specimen sintered at 400°C. The fracture morphology shown in Figure 17 shows an increased deformation in comparison to Figure 11a but less pronounced than that shown in Figure 11b.

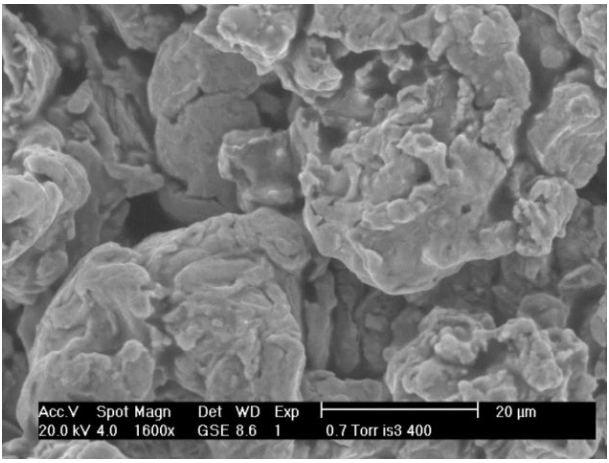

Figure 17: fracture surface of the 400°C sintered specimen applying pressure Pf at 300°C

If Pf is applied at 600°C a displacement rate peak is still observed but it is significantly smaller than that recorded when pressure is applied at 300°C since the powder is more resistant to densification.

At 900°C the application of P_f has no visible effect on displacement, since the material density is very close to 100% of the theoretical one.

Figure 18 shows the microstructure of the specimens. The grain size is tendencially smaller in the material sintered with the final pressure applied at 900°C and several annealing twins may be observed. It may be concluded that the application of the final pressure at the end of the heating step promotes recrystallization

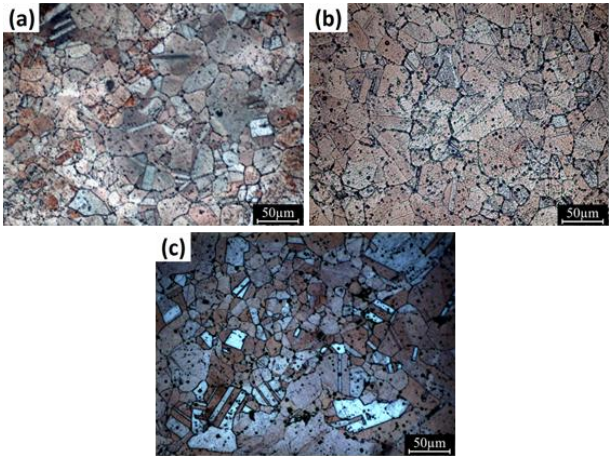

Figure 18: Microstructure of the sintered 25 - 45 µm powder applying pressure at (a) 300°C, (b) 600°C, and (c) 900°C

In all the cases, density is 100% of the theoretical one, microhardness and hardness are 64±2 HV0.05 and 81±3 HB, respectively. Therefore, the temperature at which P_f is applied does not have any effect on density and hardness, and a slight effect on microstructure. To evaluate the effective consolidation attained, and any possible effect of temperature at which the final pressure was applied, tensile tests were carried out on the 25 – 45 µm powder. The final pressure was applied at three temperatures during the heating step, around the bulk deformation peak: 300°C, 472°C and 567°C. The stress-strain diagrams under the aforementioned conditions are shown in Figure 19.

All the specimens show an extensive plastic deformation with strain a hardening and a poor localized plastic deformation. Yield Strength and Ultimate Tensile Strength are very similar, whilst percent elongation at fracture increases when P_f is applied at 472°c and 567°C (Table 5), significant of an enhanced sintering.

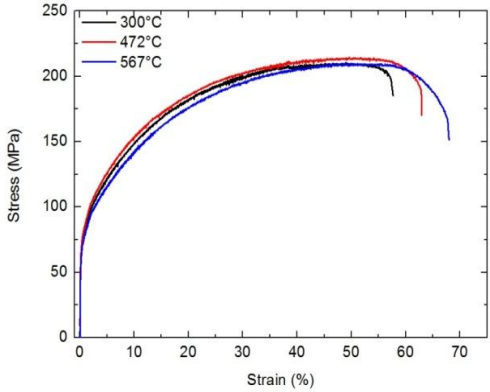

Figure 19: Stress versus strain of the SPS specimens obtained applying pressure at 300, 472 and 567°C

Table 5:Tensile properties of the specimens sintered applying Pf at 300, 472 and 567°C

Temperature (°C)	Yield Strength (MPa)	Ultimate Tensile Strength (MPa)	Elongation at fracture (%)
300	69,1	212,9	58,4
472	67,9	217,1	66,8
567	65,3	215,4	67,0

The fracture surfaces of the tensile tested specimens obtained applying P_f at 300°C and 567°C are reported in Figure 20. These specimens present a fully dimpled morphology characteristic of ductile material.

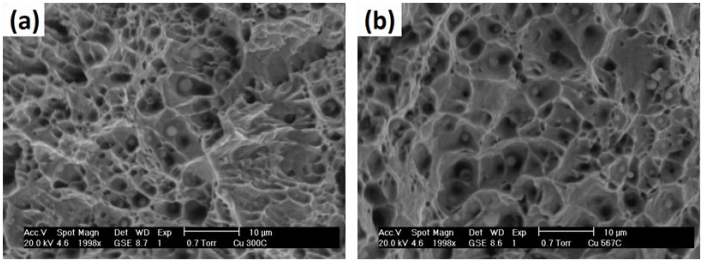

Figure 20: Fracture surface of the specimens sintered applying P_f at (a) 300°C and (b) 567°C

4.1.3. The confirmation of the surface melting of the particles

The microstructural characterization of the previous specimens does not give evidence of the surface overheating occurring during SPS, likely since it involves a very thin layer which is further deformed at high temperature. Since the thickness of the overheating layer increases with particle size, copper spheres with diameter ranging between 1 and 3 micrometers were used to produce SPS cylindrical specimens of 10 mm height and 20 mm diameter. A small pressure of 6 MPa, corresponding to the minimum force required to establish the electrical contact between punches and powder, was applied at the beginning of the SPS cycle. Temperature was increased at 100°C/min up to 780°C and 900°C, The sintered specimens were fractured, and the fracture surface was observed at the Scanning Electron Microscope (SEM). Moreover, microstructural analysis was carried out on metallographic specimens, after etching with 35 ml of nitric acid in 100 ml of distilled water solution.

Figure 21 shows the record of the current and of the nominal temperature during the SPS cycle at 900°C and the overheating profile at four different nominal temperatures.

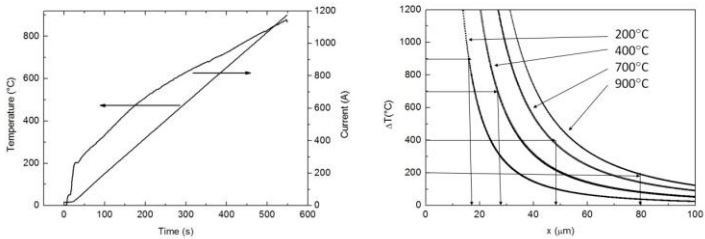

Figure 21: current intensity and nominal temperature vs time and overheating profiles at different nominal temperatures

The thickness of the layer which overcomes the melting temperature of copper is determined in the figure at the four nominal temperatures; as an example, at the nominal temperature of 200°C, a surface layer of about 18 micrometers thickness is exposed to a minimum overheating of 886°C, thus exceeding the melting point of copper (1086°C). The thickness of the supposed melted layer increases up to 80 micrometers at the nominal temperature of 900°C.

Figure 22 shows the displacement and displacement rate curves of the lower punch of the SPS apparatus. The phenomena responsible for densification are indicated in correspondence of three peaks of displacement rate: rearrangement of the particles, localized deformation at the contact points, bulk deformation of the particles as observed previously.

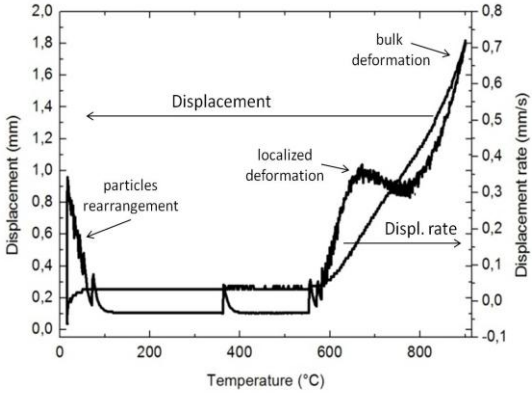

Figure 22: Displacement and displacement rate of the lower punch vs. nominal temperature

From Figure 22 it may be concluded that the large spheres undergo localized plastic deformation at about 600°C and the incipient propagation of deformation within the core of the particles at about 800°C.

The fracture surface of the specimen sintered at 900°C at different magnifications is shown in Figure 23.

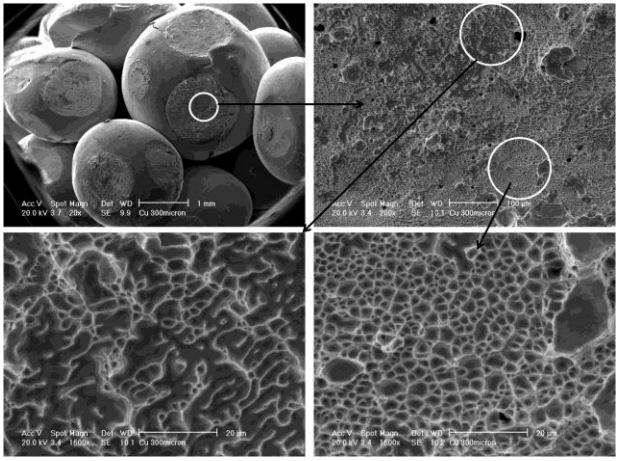

Figure 23: fracture surface of the specimen sintered at the nominal temperature of 900°C

It shows slightly deformed particles and fractured necks with two different morphologies: one cellular with only a few small dimples in the intercellular regions (bottom-left side) and another fully dimpled (bottom-right). The latter is significant of a ductile fracture, indicative of a strong bonding after sintering while the former is indicative of a weak bonding. This means that the neck has been formed with an inhomogeneous strength within its section.

Figure 24 shows two examples of the microstructure of the particles in the neck regions of the specimen sintered at 900°C, at the neck edge and in the central part.

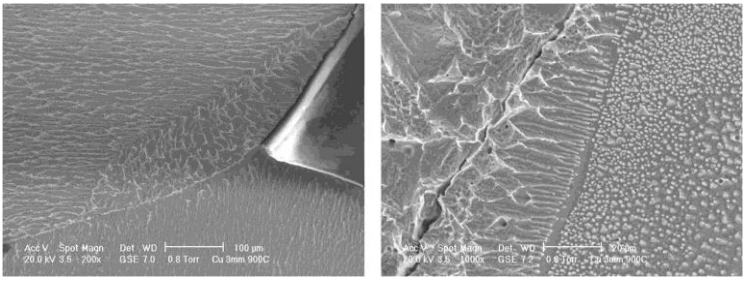

Figure 24: microstructure of the neck in the specimen sintered at 900°C

The microstructure in the neck region is coarser and differently oriented than in the bulk of the particle, within a 50-100 micrometers thick layer. Such a microstructure does not involve the whole neck and may propagate outside from the neck (left-side micrograph). In the right side image, equiaxed grains are located at the grain boundary between the two particles, from which elongated grains propagate in radial direction. Such a microstructure is similar to that formed by solidification under large undercooling. The thickness of the layer with a modified microstructure corresponds to that of the layer which had overcome the melting point of copper due to the localized overheating calculated in figure 21. Moreover the columnar grains are oriented along the direction of the overheating profile. The solidification microstructure of the contact regions and the correspondence between the thickness of the melted layer and that involved in overheating calculated from the Song model may be a confirmation of the large localized overheating induced by the pulsed continuous current.

4.1.4. Summary

The main results obtained on the atomized powder may be summarized as follows:

1. Surface overheating, above the melting point of the material, has been confirmed.

2. Densificaion and sintering mechanisms have been invstigated by measuring density and observing the fracture surface of the sintered specimens. Densification does not imply sintering necessarily; in many cases, densification occurs without an appreciable sintering.
3. SPS mechanisms are: rearrangement, local deformation, bulk deformation and sintering, occurring on increasing temperature. Effective sintering occurs at high nominal temperature, above 600°C.
4. The three variables: temperature, pressure and particle size, have different influence on density and sintering in the ranges investigated. In particular, the main effect is due to temperature, followed by particle size and pressure, which has a very poor effect. The temperature/particle size interaction has an effect comparable to that of particle size.
5. Temperature influences densification and sintering due to its effect on resistance to plastic deformation and on the mass transport phanomena responsible for sintering. The effect of particle size on densification and sintering is due to its effect on the local pressure (negligible) and electrical resistance (significant) and consequently on the overheating profile (significant). Moreover, particle size influences mass transport phenomena responsible for sintering through its effect on intraparticle grain size: the finer the particles, the larger te grain boundary surface, which results in an enhanced mass transport towards the neck region. Pressure has a negligible effect since copper is easily deformable.
6. If pressure has to be increased above the initial value to obtain a high density, it should be made at temperatures at which deformation propagates to the core of the particles (large displacement peak due to bulk deformation), to contribute to bulk deformation. Within this range, the higher the temperature value at which pressure is increased the higher tensile ductility, while density and tensile strength are not influenced.

4.2. The cryomilled copper powder

4.2.1. Grain size and dislocation density

Figure 25 shows the morphology and the XRD pattern of the cryomilled copper. The cryomilled powder (< 25 μm) has a crystallite size of 17 nm and a dislocation density of 6.25×10^{16} m^{-2} and XRD analysis reveals the presence of CuO and Cu2O in small amount, as it can be seen in Table 6.

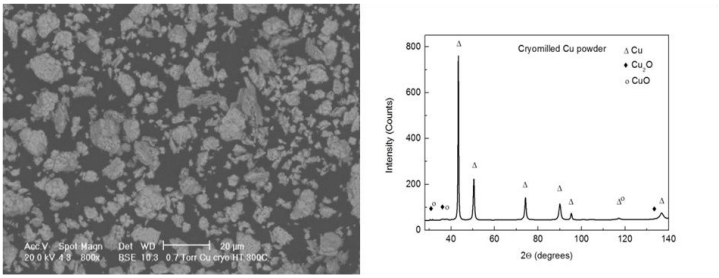

Figure 25: Morphology and XRD pattern of the cryomilled copper powder

Table 6: crystallite size, dislocation density, copper oxide content, oxygen and nitrogen content of the cryomilled powder

D (nm)	ρ_{disl} ($10^{16} m^{-2}$)	%CuO	%Cu_2O	O (%)	N (%)
17 ± 2	6,26 ± 0,04	2,0 ± 0,4	1,8 ± 0,3	1,2	0,2

4.2.2. Thermal stability

The cryomilled powder (< 25 μm) has a crystallite size of 17 nm and a dislocation density of 6.25×10^{16} m^{-2}, as measured by XRD. The high density of dislocations in the regions adjoining grain boundary is an obstacle to grain boundary mobility and contributes to the resistance to grain growth (Molinari A., 2010). The powder was heat treated in a Tersid tubular high vacuum furnace (10^{-5} mbar) at different temperatures (290, 400, 500 and 600°C) for two hours (2h) of isothermal holding. Dislocation density and grain size of the specimens treated at the different temperatures are repoted in table 7 and plotted in Figure 26 as a function of temperature.

Table 7: Grain size and dislocation density of the as-milled copper before and after 2h annealing at different temperatures

	grain size (nm)	Dislocation density ($x\ 10^{16} m^{-2}$)
As-milled	17	6,25
290°C	22	1,40
400°C	25	0,60
500°C	34	0,35
600°C	55	0,35

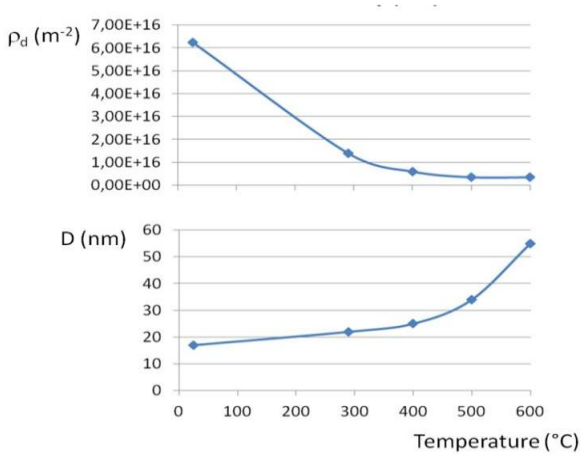

Figure 26: dislocation density and grain size of cryomilled powder vs. temperature

Dislocation density decreases noticeably just at 290°C and crystallite size increases consequently. The trend is maintained at higher temperatures but at 600°C crystallite size is still nanometric (< 100 nm), indicating quite a great thermal stability of the nanostructure. The comparison between the two graphs shows that grain size can increase only after dislocation density decreases, confirming the opposition offered by dislocations to grain boundary mobility (Moelle C. H. and Fecht H. J., 1995; Molinari A., 2010).

The structural evolution of the cryomilled powder has been investigated by DSC, and Figure 27 shows the DSC curve up to 600°C of the as cryomilled powder (upper side) and after heat treatment at 290°C (lower side).

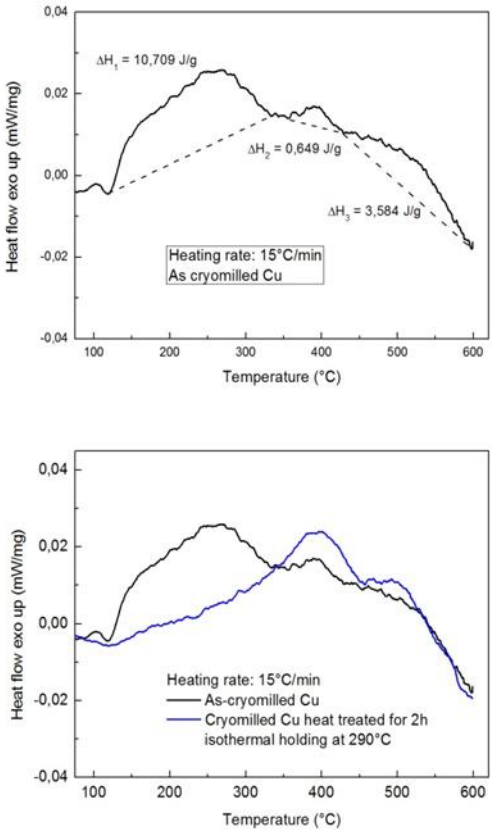

Figure 27: DSC of the cryomilled Cu before and after a heat treatment for 2h isothermal holding at 290°C using a heating rate of 15°C/min

The curve shows a sequence of exothermic phenomena over the whole temperature interval investigated. Three broad peaks can be recognized, and the enthalpy

released is 10,709; 0,649 and 3,584 J/g, respectively, corresponding to a total enthalpy released of 14,942 J/g. After heat treatment at 290°C with 2h isothermal holding, this total released energy becomes 7,684 J/g corresponding to a released energy during the previous heat treatment (corresponding to the first peak in the curve of the as cryomilled powder) of 7,258 J/g.

Energy is accumulated by the cryomilled powder in form of strain energy (linked to the large dislocation density) and grain boundary energy, and is progressively released on increasing temperature. These energies can be calculated with equations (12), (13) and (14) for energy accumulated by edge dislocations ΔH_{edge}, by screw dislocations ΔH_{screw} and grain boundary ΔH_{gb}, respectively (Zhao Y. H., 2002) **:**

$$\Delta H_{edge} = \rho_{edge} \frac{Gb^2}{4\pi(1-\nu)} \ln\left(\frac{R_e}{r_0}\right) \quad (12)$$

$$\Delta H_{screw} = \rho_{screw} \frac{Gb^2}{4\pi} \ln\left(\frac{R_e}{r_0}\right) \quad (13)$$

$$\Delta H_{gb} = 3.3 \frac{\gamma_{gb}}{D} \quad (14)$$

where:

ρ_{edge} and ρ_{screw} are the density of edge and of screw dislocations;

G is the shear modulus (4,68 x 10^{10} N/m^2);

b is the Bürgers vector (2.56 x 10^{-10} m);

R_e is the outer cutoff radius of dislocations, assumed equal to grain radius

r_0 is the inner cutoff radius of dislocations, assumed equal to the Burgers vector,

ν is the Poisson coefficient (0.364);

γ_{gb} is the specific grain boundary energy.

The grain boundary energy of a cryomilled copper powder was calculated by Zhao et al., obtaining different values depending on the milling time (0.16-0.29 J/m^2). The reason for such a variability is the occurrence of grain boundary sliding which changes the structure of the cryomilled powder. Grain boundary energy increases on decreasing grain size and dislocation density. By comparing the results of that work with those of the present investigation, a value of 0.29 J/m^2 may be assumed.

Using equations (12) to (14), the energy stored by dislocations and grain boundary was calculated in the cryomilled powder and after heat treatment at the different temperatures, assuming a constant ratio between edge and screw dislocations density equal to 1. Results are reported in table 8.

Table 8: Energy stored by dislocations and grain boundary (J/g)

	ΔH_{screw}	ΔH_{edge}	ΔH_{disl}	ΔH_{gb}	ΔH_{total}
As-milled	5,99	9,42	7,70	6,33	14,03
290°C	1,44	2,26	1,85	4,89	6,74
400°C	0,74	1,17	0,96	4,30	5,26
500°C	0,40	0,63	0,52	3,16	3,68
600°C	0,45	0,70	0,58	1,96	2,54

There is some discrepancy beween enthalpy measured by DSC and the released energy calculated from the grain size and the dislocation density at the various temperatures However, the difference between the total enthalpy released by the cryomilled powder and by that heat treated at 290°C during DSC experiments (7,258 J/g) and the difference between the calculated energy of the cryomilled powder and that heat treated (7,563 J/g) are in excellent agreement. The three exothermic peaks in DSC correspond to the progressive decrease of dislocation density and the corresponding grain growth, which seem to occur in a step-wise process rather than in a continuous one.

For a better understanding of the phenomena observed in the DSC curves, the Kissinger method was used to evaluate the activation energy, E of the first peak shown in Figure 28.

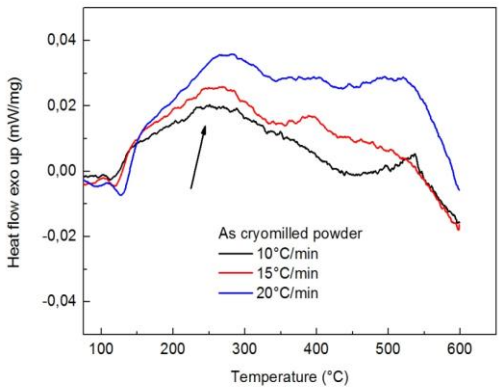

Figure 28: : Variation of the exothermic DSC curves of the as-cryomilled copper measured at different heating rates: 10, 15 and 20°C/min

In this method the variation of the maximum peak temperature (reported in Table 9) with the heating rate is studied according to the following equation:

$$Ln\left(\frac{\beta}{T_p^2}\right) = -\frac{E}{RT_p} + C \qquad (15)$$

where β is the heating rate, R the gas constant (8,314 J mol-1.K-1) and Tp the maximum peak temperature.

Table 9: Values of the peak temperature of the cryomilled copper at different heating rates (10, 15 and 20°C/min) shown in Figure 28

Heating rate (°C/min)	10	15	20
Peak temperature (°C)	251,033	268,533	282,066

The plot of $\ln(\beta/T_p^2)$ versus $1/T_p$ shown in Figure 29, gives a straight line from the slope of which is derived the activation energy which is calculated to be 6,28 kJ/mol

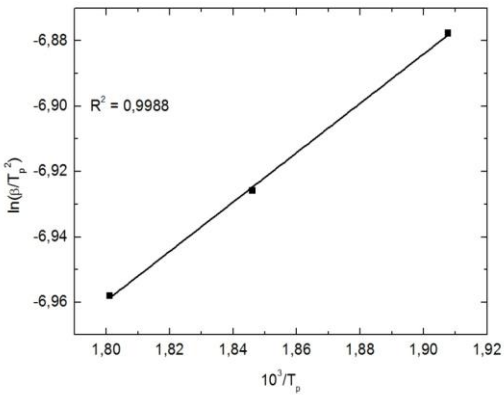

Figure 29: Kissinger plot of the values of $\ln(\beta/T_p^2)$ as a function of $1/T_p$ calculated from Table 9

This value is very low as compared, for instance, to that obtained by S Simoes et al. (Simões S., 2010) who measured an activation energy for grain growth of 35 kJ/mol. The main phenomenon observed in this temperature range is the decrease of dislocation density, which is responsible for about 80% of the energy released, according to calculation reported in Table 8. The high dislocation density accumulated during the cryomilling process leads to a highly unstable condition

which makes the stored energy easy to be released, to let the material recover a stable a state through dislocation recovery, stress relaxation and grain boundary reordering. Roy et al. (Roy I., 2006) explained the low activation energy involved as indicative of the highly unstable grain boundaries that need only a small additional driving force to enable rearrangement of grains and grain boundaries. The low activation energy can also be attributed to the enhanced atomic mobility of the non-equilibrium grain boundaries due to the increased diffusivity arising from the presence of many extrinsic dislocations. The calculated activation energy is smaller than that reported by Siddiqui (Siddiqui R. A., 1991) for defects annihilation in a cold worked copper, but the structrural defectiveness of a cryomilled nanostructured copper is much more pronounced that of a cold worked material.

The activation energy of the second DSC peak was calculated, too, by carrying out DSC measurements of the cryomilled and 290°C heat treated powder at three different heating rates (15, 20 and 30°C/min). Results are shown in Figure 30 and Table 10.

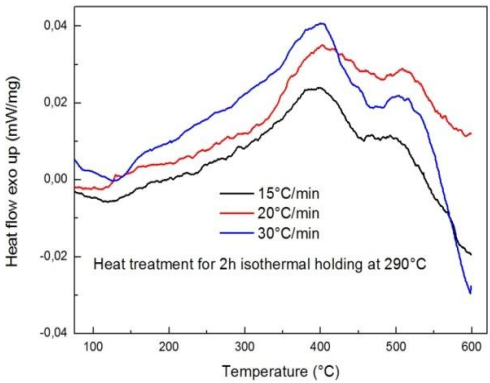

Figure 30: Variation of the exothermic DSC curves of the cryomilled copper after heat treatmenet for 2h isothermal holding at 290°C measured at different heating rates: 15, 20 and 30°C/min

Table 10: Values of the peak temperature of the cryomilled copper at different heating rates (15, 20 and 30°C/min) after 2h isothermal annealing at 290°C of the DSC curves in Figure 31

Heating rate (°C/min)	15	20	30
Peak temperature (°C)	399,787	402,4	405,037

Activation energy is 25,44 KJ/mol, comparable to that obtained by Siddiqui et al. (Siddiqui R. A., 1991) for defects removal. The phenomena occurring in this temperature range are the decrease of dislocation density and grain growth, which give a comparable contribution to the energy released according to calculation in Table 8. This would confirm that the decrease of the defect density is the controlling phenomenon for grain growth.

The calculation of the activation energy of the third peak in DSC curves failed, since the three experimental points do not depict a linear trend in the $\ln(\beta/T_p^2)$ versus $1/T_p$ diagram.

4.2.3. Contamination and degassing behaviour

The cryomilled powder is contaminated by nitrogen and oxygen, which form unstable compound (Wen H., 2011). Figure 27 shows the results of DSC and TGA measurements, along with the records of the displacement of the lower punch and of the chamber pressure during SPS. It has to be considered that the DSC/TGA machine is much less sensitive than the DSc equipment used for the study of thermal stability of the powder reported in the previous section. Therfore the exothermic peaks due to the evolution of dislocation density and grain size are not revealed by the experiments reported in this section.

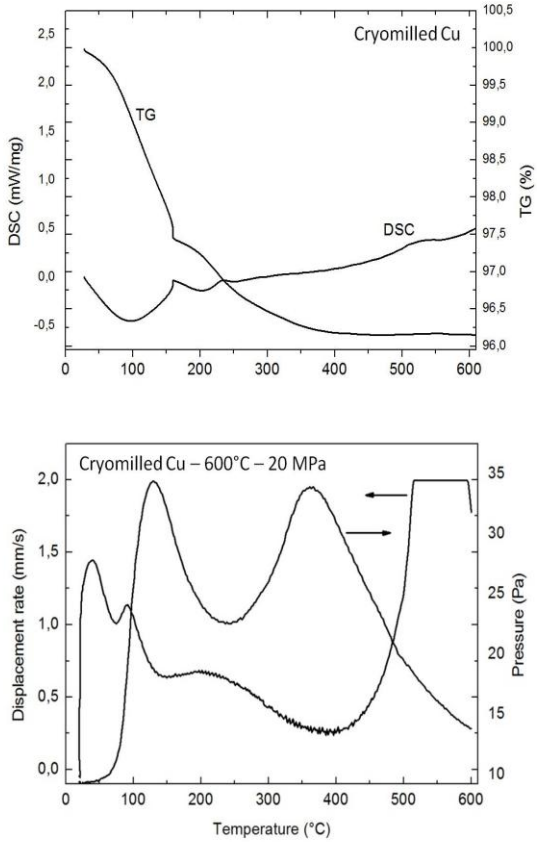

Figure 31: Degassing curves in TGA-DSC and effect on the SPS chamber pressure

A sharp mass loss occurs up to 400°C, to which two exothermic effects are correlated in DSC record. These effects may be attributed to the destabilization of $Cu(NO_3)_2$, occurring below 300°C, and of Cu_3N around 300°C (Wen H., 2011). The gaseous products released by the two reactions increase the pressure in the SPS chamber, which opposes densification as shown by the decrease of the displacement rate reported in the figure below. A third enthalpic effect is shown by

DSC curve at 520-550°C. It is attributed to the reduction of CuO, according to reaction $4CuO = 2Cu_2O + O_2$, which occurs at 520°C (Wen H., 2011). The reduction of copper oxide may occur at a lower temperature in a hydrogen atmosphere (Sakka, 1989), but it is retarded in the SPS chamber where no reducing gases are present. It is interesting to observe that no mass loss is measured by TGA, which means that oxygen remains entrapped in the nanostructured copper as interstitial atom due to the enhanced solubility promoted by dislocations which are present in a large amount even at 500-550°C (Table 8).

Impurities form atmospheres around extensive defects and through their nature and size as well the position they occupy within the material control the motion of dislocations (Sobol' V. R., 2007) by blocking the migration of vacancies. In the case of oxygen atoms which have strong binding to both screw and edge dislocations due to their asymmetric elastic distortions, strong Cottrell locking (atmospheres) can take place (Prasad Y.V.R.K., 2004) preventing dislocation core diffusion to occur. The oxygen content in solution is higher enough (Prasad Y.V.R.K., 2004) to block dislocation pipe diffusion and activate lattice self-diffusion which is responsible for dislocation climb. This implies a high stress to move dislocations. The continuous decomposition of copper oxide and the release of oxygen as temperature is raised may play an important role in partially allowing dislocations to move and leading to the presence of different types of deformation mechanism during the sintering process.

According to the results of DSC and TGA experiments, it has been decided to delay the application of pressure during SPS above the degassing temperatures. Therefore, pressure was applied at 450°C.

4.3. SPS of the cryomilled copper powder

4.3.1. A DOE study of the effect of temperature, pressure ans particle size

The particles which are shown in Figure 32, have a flake-like morphology, due to the insufficient milling time. It is well known in fact that particle size gets rounded in the final stage of milling.

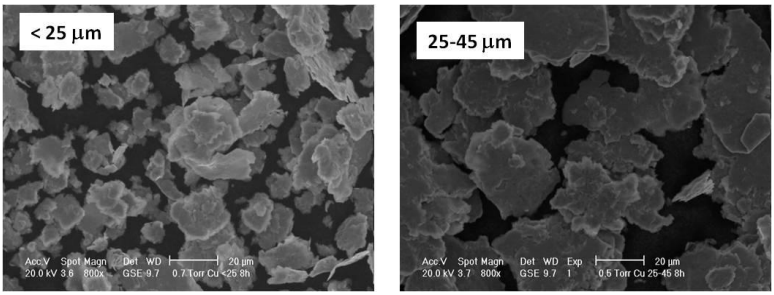

Figure 32: morphology of the cryomilled powder

The cryomilled powder has a crystallite size of 17 ± 2 nm and a dislocation density of 6.25 ± 0.04 x 10^{16} m^{-2} m^{-2} in both the particle size utilized. Since the crystallite size depends on particle size, this result would suggest that particles are actually agglomerates of different sizes of much finer particles.

The DOE approach was implemented on the cryomilled copper as previously described in paragraph 4.1.1. using the data shown in Table 11

Table 11: Density and crystallite size of the sintered DOE specimens

Experiment	Ps	T	P	ρ (g/cm^3)	ρ (%)	D (nm)
1	-	-	-	7,23	81,4	36
2	+	-	-	7,42	83,2	36
3	-	+	-	7,86	88,2	42
4	+	+	-	7,91	88,7	42
5	-	-	+	7,72	86,5	37
6	+	-	+	7,81	87,5	34
7	-	+	+	8,14	91,3	34
8	+	+	+	8,18	91,7	36

Full density was not obtained in the sintering conditions utilized. On the other side, the differences in crystallite size are quite small and a mean crystallite size of 38±4 nm can be assumed, irrespective to the three factors investigated. SPS does not densify the powder completely but the nanostructure is preserved.

Fig. 33 compares the main effects of the three different factors on density as well as the interaction between them. In Fig. 33a, temperature appears to be the most important factor on density. It is followed by pressure which also has a high effect. Particle size has a very small effect compared to temperature and pressure.

This poor effect of particle size combined with the similar crystallite size mentioned above confirms that the particle size is actually the same and smaller than expected. Particles are agglomerated and the two particle sizes considered here are definitely agglomerates with different size. Therefore it may be concluded that agglomerate size has the minor effect on density.

The interaction plot between agglomerate size and temperature is shown in Fig. 33b. Density increases with temperature and there is a very poor interaction between these two factors; it seems that temperature is slightly more effective on the fine agglomerates. Fig. 33c shows the interaction plot between agglomerate size and pressure. Density increases with pressure and, in this case, the interaction is negligible. This means that the resistance to fragmentation of the agglomerates is

similar for both sizes. The interaction plot between temperature and pressure is also shown in Fig. 33d. Here the interaction is appreciable. Pressure is more effective when increased at low temperature level. On the other side, on increasing temperature from low to high level, density performs better at low pressure level. Temperature and pressure have a slight synergic effect.

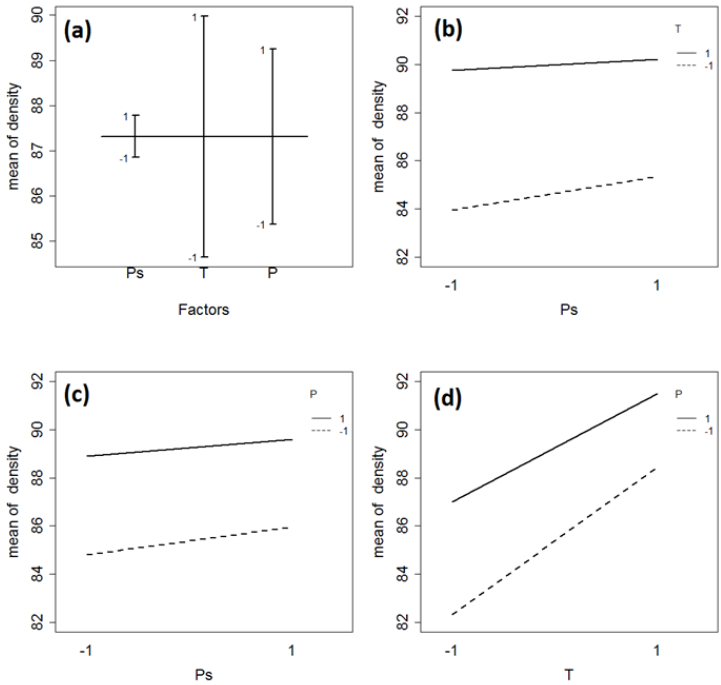

Figure 33: Main and interaction plots of particle size, temperature and pressure on density

The effect of agglomerate size, temperature and pressure on density can be observed on the displacement curves collected during SPS, i.e. the curves representing the movement of the lower punch, shown in figure 34.

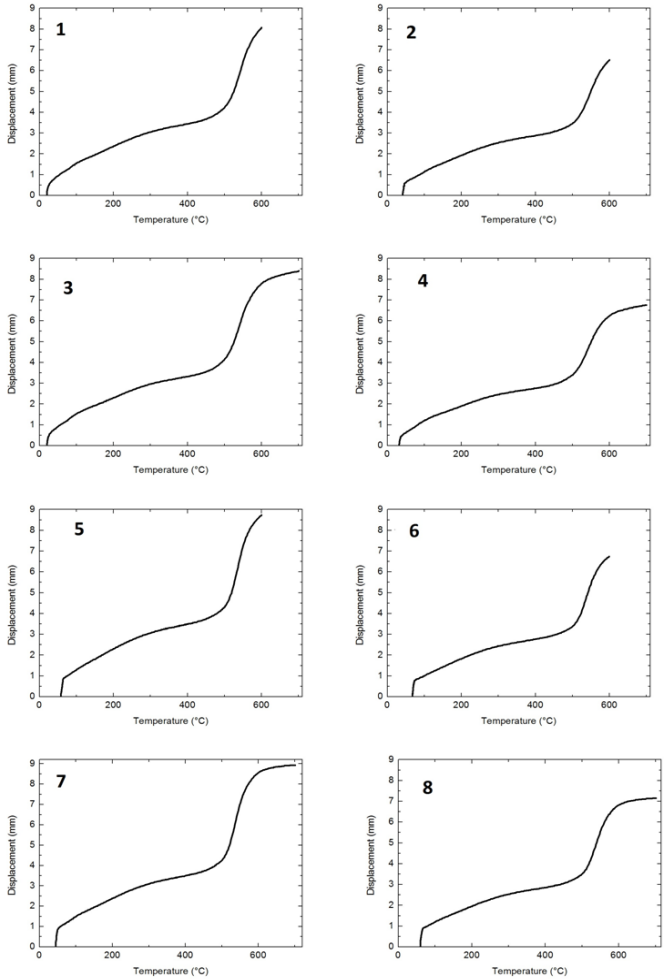

Figure 34: Displacement curves of specimens produced with the fine particle size (label refer to Tab. 11)

In a previous section on the atomized powder, densification mechanisms have been investigated and correlated to the shape of the displacement curve. Most of

densification occurs during the heating step by rapid particle rearrangement at the beginning, followed by localized deformation at the contact points and by bulk deformation of the particles. The displacement peaks of localized and of bulk deformation are clearly visible in the temperature range between 300-600°C. Temperature enhances plastic deformation through thermal softening. Densification is not accomplished by sintering, which occurs at higher temperature, still during heating, by power law creep. On increasing particle size, rearrangement and deformation is enhanced, while power law creep is retarded.

The curves in Figure 34 show a gradual increase in displacement with temperature and a sharp increase when pressure is applied. Densification of nanostructured powders is expected to be rather different because of the great resistance to plastic deformation. Instead, agglomerate fragmentation is expected to occur after rearrangement.

The curves of specimens 1 and 2 show that on increasing agglomerate size the total displacement decreases but, since final density is slightly higher for the larger agglomerates, the difference in displacement may be attributed to the different apparent density of the powder. On increasing agglomerate size, apparent density increases and the displacement to obtain the same final density decreases consequently.

The comparison between specimens 1 and 3 (same agglomerate size and same pressure) shows that on increasing temperature displacement increases slightly, since the slope of the curves above 600°C decreases significantly. The comparison between specimens 1 and 5 (same agglomerate size and temperature) shows that the increase in pressure enhances displacement, as it was expected.

Total displacement of specimen 3 is lower than that of specimen 5, while final density (Table 11) is the opposite. The reason for this incoherency may be the larger springback occurring when pressure is released at the end of the SPS cycle in specimen 5, because of the larger elastic recovery.

The effective consolidation (effective sintering) of the powders can be evaluated by the fracture surface of the specimens. All the specimens were broken and fracture surfaces are shown in Figure 35.

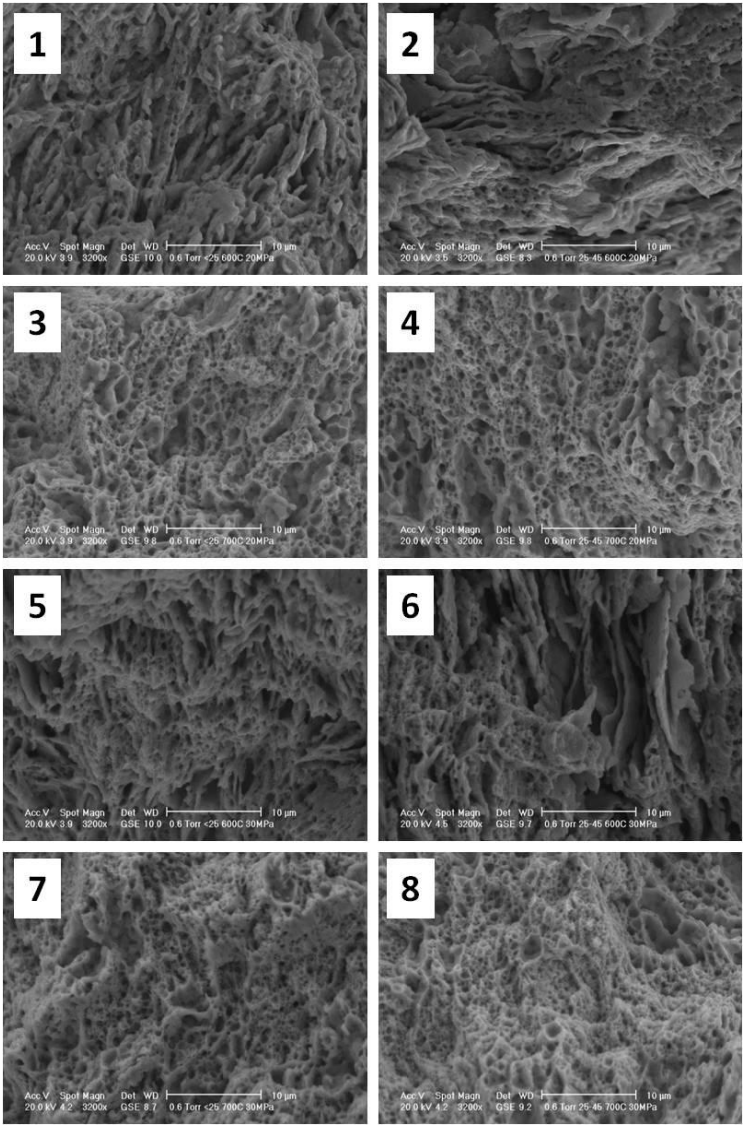

Figure 35: fracture surfaces of the sintered specimens (label refers to codes in tab. 11)

The fracture morphology shows both dimpled areas and areas where the flake-like morphology of the starting powder is visible. Dimples are significant of a ductile fracture and, in turn, of bonding occurred between particles. On the other side, flake-like morphology recalls the structure of the cryomilled powder and is significant of lack of bonding: fracture occurred by interparticle propagation of cracks.
The figure shows that fracture is practically 100% dimpled in high temperature sintered specimens, while in the other it is mixed, with prevailing flake-like morphology. No evidence of the effect of the other parameters may be observed. This means that the parameter promoting effective sintering is temperature. With reference to the displacement curves, it may be concluded that along the low slope final step in specimen 3 (where temperature increases from 600°C up to 700°C) consolidation occurs, while along the high slope final step in specimen 5 (where pressure increases from 20 MPa up to 30 MPa) only further densification occurs.

The current flow during the spark plasma sintering is material dependant through the statistical distribution of the grains as well as their size and the nature of their contact (shape and properties). The applied pressure, which is highly affecting the deformation mechanism, is strongly affecting the current flow. As current flows in the material through the contact between grains, its effectiveness is determined by both the applied pressure and the properties of the material at the contact zone (Eric Falcona, 2005).
Figure 36 shows the plots of current vs. voltage (a) and of temperature vs. current (b). This behavior of the Current/voltage curve is significant of the electrical conductivity transition in granular materials which depends on the statistical distribution of the shape and size of the particles, the applied force, and the local properties at the contacting zone between particles (degree of oxidization, surface state and roughness) (Eric Falcona, 2005). On increasing voltage, current/voltage curve increases exhibiting three main phenomena. The frist phenomenon is an Ohmic (linear) behavior up to about 1.6 V and 300 A, indicating a constant resistance, without any significant change in temperature (Figure 36 (b)).

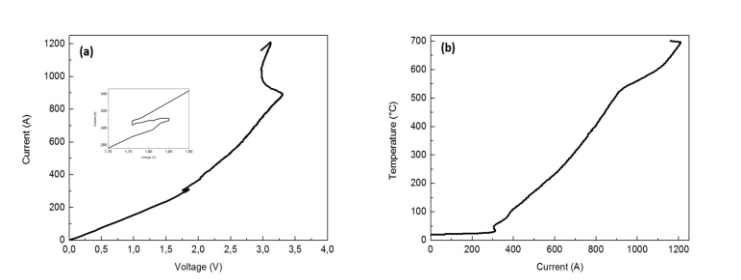

Figure 36: (a) current versus voltage and temperature versus current (b) records during SPS of cryomilled powder

This is a characteristic of samples behaving as ohmic resistors in which the current density is controlled by thermally generated electric fields, across the gap between the conductive particle (El-Tantawy, 2002). This insulative behavior is attributed to the presence of copper oxide. At a voltage of around 1.8 V, as shown in the inset of Figure 36(a), it may be observed a decrease of voltage with a constant current intensity, resulting from a decrease of the resistance of the material. This unstability indicates the breakdown of oxide, since the electrical resistance depends on the material properties (resistivity and thickness) at the contact location (Eric Falcona, 2005). Only after this breakdown current starts flowing through the metallic particles, heating up the material (as shown by the temperature jump in Figure 36(b)). Above this threshold, temperature increases and the two curves (voltage/current and curren/temperature) have a stable behavior. On increasing voltage the material behavior changes from Ohmic to non-Ohmic and the curves become concave, which is significant of a continuous decrease of resistance. This is due to the continuous increase in the contact areas between copper particles, the creation of new electrical paths (Dorbolo S., 2003) (Dorbolo S., 2007), and the increase in conductivity as temperature is rised. The third effect occurs at 3.7 V when temperature reaches 500°C, the temperature at which pressure is applied. This event causes a destabilization in the voltage/current curve and decreases the heating efficiency

(decrease of the slope of the current/temperature curve) since electrical resistance decreases fast due to the sharp increase of the contacting area as a result of the increased pressure..

4.3.2. The effect of the nanostructure on densification and sintering mechanisms

Figure 38 shows the atomized and the cryomilled powders with the same granulometry (< 25 μm): the former has the typical rounded morphology of gas atomized powders whilst the latter has a flake-like morphology.

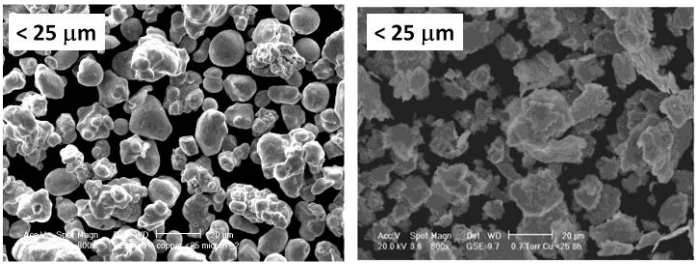

Figure 37: the atomized and the cryomilled powder (particle size below 25 μm)

The high dislocation density (ρ_d = 6.26 ± 0.04 x 10^{16} m^{-2}) typical of nanostructured materials obtained by milling enhances the solubility of oxygen as an interstitial atom, due to the low activation energy for the formation of Cottrel atmospheres (Prasad Y.V.R.K., 2004). This may justify the absence of copper oxides peaks in the XRD spectrum.

Figure 38 shows the displacement curve of the cryomilled powder in comparison to that of the atomized one when the two powders are sintered at 600°C with a final pressure of 20 MPa applied at 450°C.

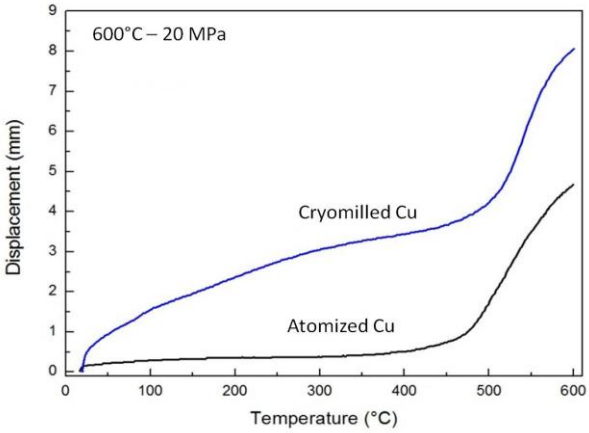

Figure 38: Displacement curve of the cryomilled and of the atomized powder

The displacement of the upper punch during SPS of the cryomilled powder is greater than that of the atomized one. A contribution to the larger displacement may be due to the more irregular morphology of the particles shown in Figure 38, which decreases its apparent density and, in turn, increases the filling height in the die cavity, as actually measured. Under the application of the initial pressure the packing of the cryomilled particles and, in turn, their displacement, are therefore more pronounced. This effect is responsible for the sharp shrinkage at the beginning of the SPS cycle and may influence the whole of the curve, at least until the final pressure is applied. However, density of the two sintered specimens is 7.2 g/cm^3 (cryomilled) and 6.2 g/cm^3 (atomized), which indicates that densification is much larger for the cryomilled powder. The grain size of the cryomilled specimen is 42 nm, confirming the thermal stability of the nanostructure.

To evaluate the effective consolidation attained at 600°C, Figure 40 compares the fracture surface of the two specimens.

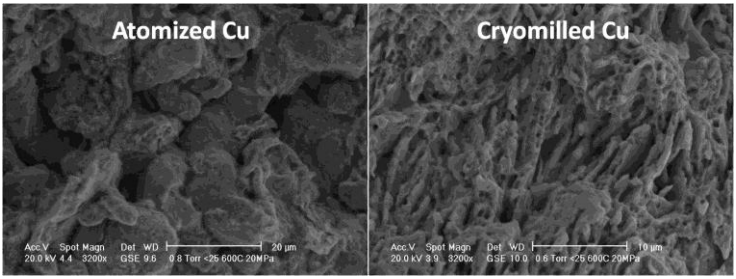

Figure 39: fracture surface of the atomized and the cryomilled specimens, sintered at 600°C

The cryomilled specimen shows several dimples on the fracture surface, indicative of a ductile fracture and, in turn, of an effective consolidation (sintering) attained. On the contrary, the atomized specimen does not show any evidence of the typical ductile behavior of copper, since fracture has been propagated along the prior particle boundaries, indicating a poor consolidation. In other words, the cryomilled specimen is effectively sintered whilst the atomized one is densified but not effectively sintered. Moreover, whilst atomized particles are deformed, in the fracture surface of the cryomilled specimen the original morphology of the flake particles may be still recognized, indicative of a poor deformation. As a confirmation of the different sintering occurred in the two specimens, figure 40 shows their microstructure.

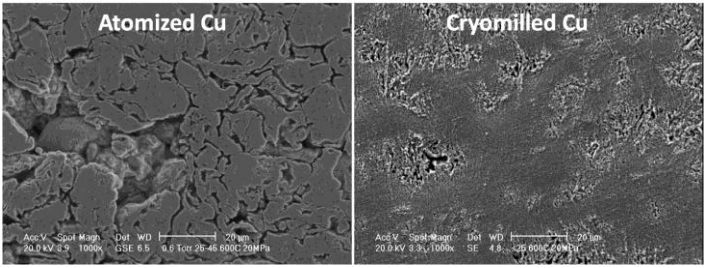

Figure 40: microstructure of the atomized and the cryomilled specimens sintered at 600°C.

There is a great difference between the particle contact regions. They are clearly visible in the atomized specimen, where only a few sintering necks can be recognized and particles are mostly in a close mechanical contact. On the other side in the cryomilled specimen necks have been formed and grown and no evidence of the original contacts is shown. The correlation between the microstructures and the morphology of the fracture surface is well evident.

The sintering mechanisms in the case of the atomized powder have been investigated and described in section 4.1. The consolidation of the material occurs through the sequence of four steps on increasing temperature: (i) rearrangement of the powder articles, (ii) plastic deformation at the contact points, (iii) bulk plastic deformation of the particles and (iv) effective sintering. The three first steps promote essentially densification but sintering starts only at high temperature, above 700°C. In other words, particles are first deformed and then extensively sintered. In the cryomilled specimens sintering starts at a much lower temperature, whilst particles are only slightly deformed. This means that the consolidation process is effectively influenced by the high mechanical strength, which retards plastic deformation, and by the enhanced sinterability, which activates the mass transport phenomena responsible for the formation and growth of the neck.

Spark Plasma Sintering is characterized by a peculiar heating mechanism promoted by the pulsed continuous current flowing through the particles. The contact regions

are exposed to a large superheating which may lead to localized melting (Song X., 2006; Yanagisawa O., 2003). Such an overheating may be calculated by Equation (10) proposed by Song et al. (Song X., 2006) assuming:

ρ = resistivity (1.67 x 10^{-5} Ω.m for atomized copper and = 3.58 x 10^{-8} Ω.m for cryomilled copper)

ρ_m = theoretical density (8.9 g/cm^3, neglecting the influence of interstitial oxygen in the cryomilled powder)

C_v = specific heat (24.44 JK^{-1}mol^{-1} for atomized copper and = 26 JK^{-1}mol^{-1} for cryomilled copper)

Φ = the inner diameter of the die (20 mm)

r = the particle size (12.5 mm, mean particle size)

The current I_s is very similar between the two specimens as shown by the curves recorded during the SPS cycle reported in figure 41.

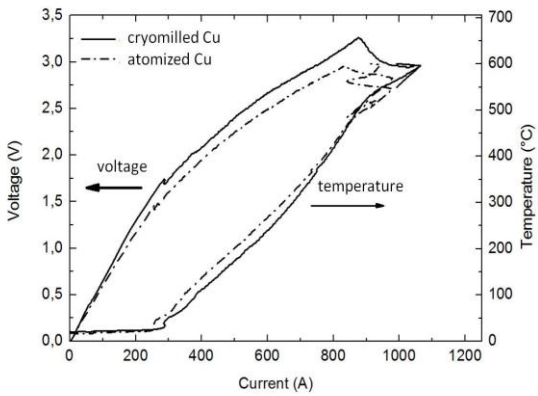

Figure 41: voltage and temperature vs. current

Figure 42 shows, as an example, the overheating profile calculated at a nominal temperature of 450°C, the temperature at which the final pressure is applied.

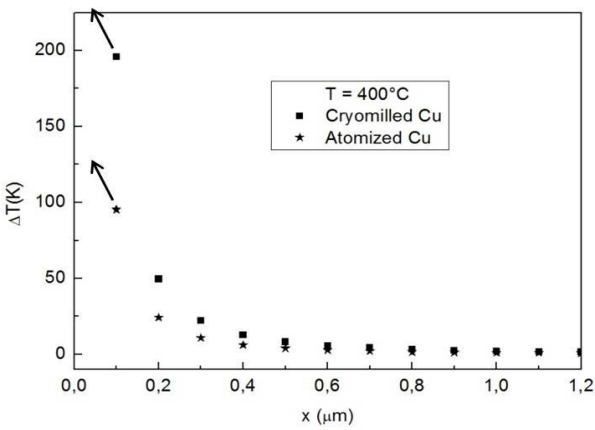

Figure 42: overheating profile in the two specimens

Overheating is more pronounced in the cryomilled specimen, because of the higher resistivity of the nanostructured material, but it is confined within a very thin surface layer in both cases, becoming negligible at 0.2 μm depth. At 600°C the difference between the two specimens is very similar to that calculated at 450°C. However, a great difference exists in terms of grains contained in the overheated layer: only a fraction of grains in the atomized material, hundreds of grains with a large dislocation density in the cryomilled material.

Overheating causes local melting, activates plastic deformation due to thermal softening of the material and enhances mass transport mechanisms. Local melting is expected to be similar in the two materials, but it cannot be observed due to the very thin layer involved. The atomized powder particles appear more deformed than the cryomilled ones, therefore plastic deformation should not have an important effect on the activated consolidation of the cryomilled specimen. Mass transport mechanisms are mainly lattice and grain boundary diffusion, plastic flow and viscous flow (Xiong Y., 2012; Liu D., 2012). Diffusivity is strongly activated by nanostructure. In presence of a large density of dislocation, the pipe dislocation diffusion

mechanism may be activated (Shima Y., 2002), and an effective volume diffusion coefficient D_{eff} may be calculated using the following equations (Shewmon, 1989)

$$D_{eff} = D_v (1 + g (D_p/D_v)) \quad (12)$$

$$g = (a/Z)^2 \quad (13)$$

$$Z^2 = \rho_d^{-1} \quad (14)$$

where D_v is the volume diffusion coefficient in presence of an equilibrium concentration of dislocations, g is the fraction of atoms belonging to dislocations, D_p is the pipe diffusion coefficient (four to five orders of magnitude greater than D_v (Shima Y., 2002) a is the radius of the pipe (0.5 nm), Z is the mean spacing between dislocations and ρ_d is dislocation density. The fraction of atoms in the cryomilled powder belonging to dislocations is 0.01 and 0.001 when dislocation density is 6.26 x 10^{16} m^{-2} (room temperature) and 0.5 x 10^{16} m^{-2} (450°C, when the final pressure is applied), respectively, and the effective diffusion coefficient of the cryomilled material is from two to one order of magnitude larger than that of the atomized one. All these dislocations are in principle scarcely mobile, even because of the drag stress exerted by the Cottrel atmospheres mentioned above (Hill, 2009); therefore the source-sink mechanism responsible for dislocation activated plastic deformation in nanostructured materials (Meyers M.A., 2006) is unlikely. On the other side, the large grain boundary surface may contribute to mass transport by grain boundary diffusion.

4.3.3. Influence of heating rate on grain size

4.3.3.1. Applying only an initial pressure P_i

This study was carried out on the cryomilled powder after degassing at 300°C for 2 hours . The measured crystallite size by XRD was 19 nm and dislocation density

4,77 x 10^{15} m^{-2}. These values are different from those reported in Table 7 since the powder utilized is not the same as that of those experiments. This fact highlights some criticism in the repeteability of cryomilling which should be investigated in depth in view of any practical application of the process. SPS was carried out at 900°C under the application of the initial pressure only.

Table 12 reports density, mean crystallite size, dislocation density and microhardness of the specimens sintered with different heating rates: 50, 100 and 150°C/min.

Table 12: Measured density, calculated theoretical density, relative density, crystallite size, microhardness and hardness and the sintered material using heating rates of 50, 100 and 150°C/min

Heating rate (°C/min)	ρ (g/cm^3)	Cu_2O (%)	ρ/ρ_{th} (%)	D (nm)	ρ_d (x10^{14}m^{-2})	HV0,05
50	8,2	4,3±0,8	91,7	38	4,26±1,79	143,0±2,9
100	8,1	6,8±0,8	91,4	48	6,37±2,82	142,6±3,9
150	8,1	3,6±0,6	91,3	67	3,99±1,86	142,9±2,8

Density and dislocation density do not change with heating rate (differences between the mean values of dislocation density are smaller than the scatter band) whereas crystallite size is definitely affected by heating rate. The mean crystallite size increases with heating rate while microhardness remains unchanged.

The crystallite size distribution obtained using PM2K software (Leoni M., 2006) is shown in Figure 43, compared to that of the cryomilled and degassed powders.

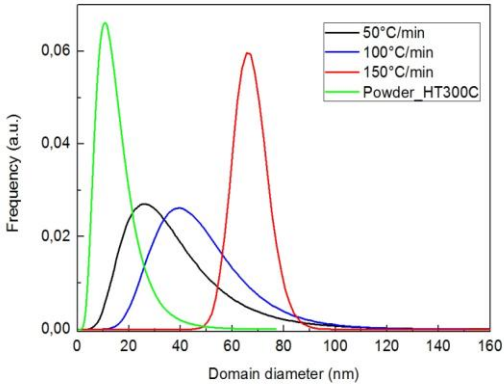

Figure 43: Domain size distribution of the heat treated powder at 300°C and of the specimens sintered with different heating rates: 50, 100 and 150°C/min applying only the initial pressure

The crystallite size distribution shifts to high values as the heating rate is rised and gets narrower at 150°C/min. In other words at 150°C/min the size distribution tends to uniformize through grain growth.

The overheating temperature profile of the three specimens sintered with different heating rates is shown in Figure 44

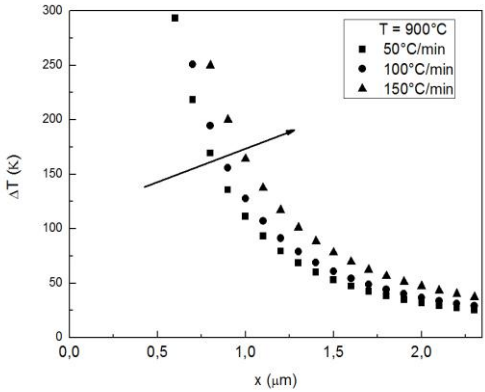

Figure 44: Effect of heating rate on the overheating profile

The local overheating increases slightly with heating rate, in terms of both actual values of temperature and thickness involved. The increase in grain size with heating rate cannot be simply justified by the different overheating profiles, since they involve a very thin surface layer of the particles and differences are not so large. It has to be considered that the reported temperature is that measured in the die wall thickness, which is lower than the actual one within the powder (Zavaliangos A., 2004), which depends on the current flowing through the material. Figure 46 reports the current vs. temperarture curves, and shows how the current intensity had to be increased to increase heating rate . This may result in a larger actual temperature to which powders are exposed during SPS and, in turn, in grain growth. There is a qualitative correspondence between the increase in current and the increase in grain size.

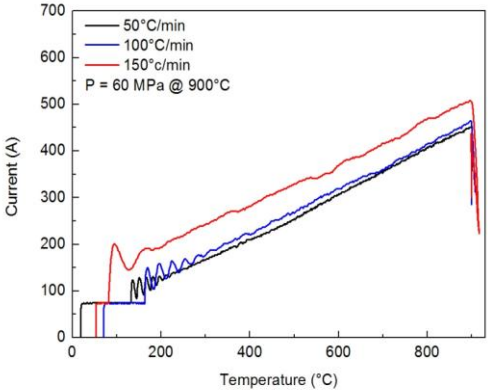

Figure 45: Currect versus temperature curves

The fracture surface of the three specimens is presented in Figure 46.

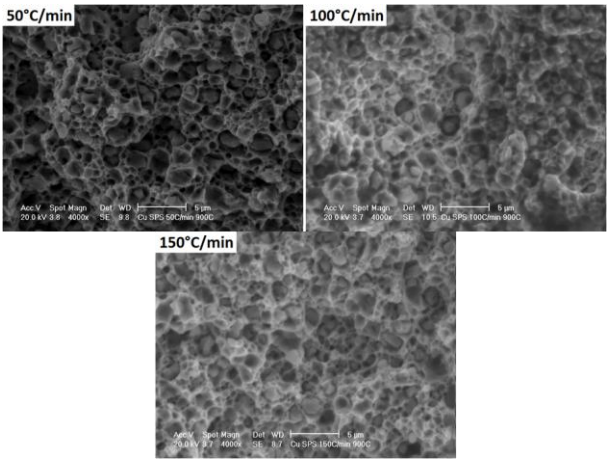

Figure 46: fracture surface analysis of specimens sintered with different heating rate

In all the cases, a fully dimpled morphology is observed, typical of ductile fracture. Many rounded particles are visible, which are supposed to be copper oxide formed

due to the recombination of oxygen with copper at high temperatures. XRD analysis of sintered specimens indeed reveals peaks pertaining to copper oxide, as shown in Table 12.

4.3.3.2. Applying final pressure at 900°C

To improve density pressure was increased up to 60 MPa at 900°C for 2 min. Table 13 shows the XRD quantitative phase analysis from which was derived the theoretical density, the measured density, crystallite size and dislocation density.

Tabella 13: Measured phase composition (QA) by XRD and derived theoretical density, measured density, relative density, crystallite size and dislocation density of the sintered material produced using heating rates (HR) of 50, 100 and 150°C/min

Heating rate (°C/min)	QA (Cu_2O, %)	Density (g/cm^3)	Theoretical density (g/cm^3)	Relative density (%)	Mean grain size (nm)	Dislocation density (10^{15} m^{-2})
50	10.7±1	7.90	8.48	93.13	52	2.78 (1.50)
100	11.9±1	7.93	8.43	94.05	58	1.84 (0.61)
150	11.7±1.1	7.88	8.44	93.40	58	2.44 (1.33)

The amount of oxide in the sintered specimens is higher than in the previous case; this leads to a lower theoretical density and therefore the final density is higher than in the previous case. Therefore, the application of the final pressure increases the formation of oxides and enhances densification. The increase in the oxide content when the final pressure is applied may by interpreted as follows. A large amount of interstitial oxygen is maintained in solid solution in the cryomilled powder by the large density of dislocations, in form of Cottrel atmospheres. When dislocation density decreases on heating, a large portion of oxygen is released either forming copper

oxide or leaving the material as a gaseous phase. On applying the final pressure, such a degassing is impaired, and a larger amount of oxide particles are formed.
Grain size is not influenced by heating rate and, a part from the specimen sintered at the higher heating rate, is larger than in the previous case. Dislocation density is one order of magnitude higher than in the previous case. The application of the final pressure homogenizes grain size and increases the density of line defects.
The increase of pressure at the sintering temperature may cause dislocations pile-up near the grain boundaries and give rise to a high stress field which may create new dislocations. This may explain the increased of dislocations density and its independence on heating rate.

The crystallite size distribution is presented in figure 47.

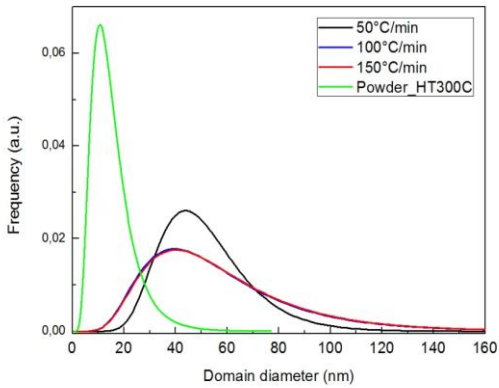

Figure 47: Domain size distribution of the heat treated powder at 300°C and of the specimens obtained using different heating rates: 50, 100 and 150°C/min applying both initial and final pressure

On increasing heating rate The grain size distribution is in principle is very similar in the three cases slightly broaden from 50 to 100°C/min and then does not change

further, but. The trend is different from the previous case (Figure 43). The size distribution at 100°C/min matches with that at 150°C/min and broaden slightly as compared to the case where only the initial pressure is applied while the mean crystallite size shifts to lower values.

The similarity of the three specimens, despite of the different heating rate, in terms of both grain size and dislocation density suggests that the final structure is determined by the effect of the final pressure applied at 900°C, which predominates on that of heating rate. Dynamic recrystallization (Zhang X., 2004) may be responsible for the increased grain size but it should result in a decrease of dislocation density. The larger grain size combined with a greater dislocation density might be explained by assuming the occurrence of a geometrical coalescence of grains following grain rotation, which is one possible deformation mechanism of nanostructured materials. This is a hypothesis which has to be confirmed.

Figure 48 shows the fracture surface of the three specimens.

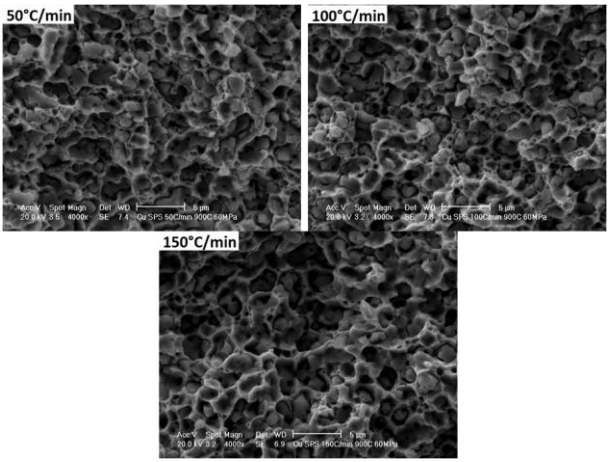

Figure 48: Effect of heating rate with a previous degassing and applying both initial and final pressure: fracture surface analysis

The fracture surfaces are still fully dimpled with the inclusion of copper oxide particles; their amount is greater than in the fracture surfaces of the previous specimens, confirming the larger amount of oxide particles in the sintered specimens. Deformation around these particles is more pronounced than in the previous case; such an increasd deformability might be significant of a better ductility promoted by the application of the final pressure . It is important to recognize that copper oxide particles play a role in causing the formation of the ductile crack but, at the same time, they have a positive effect on the crystallite size since they can prevent the structural coarsening.

In order to have a better insight on the grain size distribution, TEM analysis was carried out. The TEM observation evidences a heterogeneous structure as shown in Figures 49, 50 and 51: from very fine grains up to large grains, above 100 nm. This observation is very important, since XRD is sensitive to grain size below this threshold, which means that large grains are not included in the distribution shown previously.

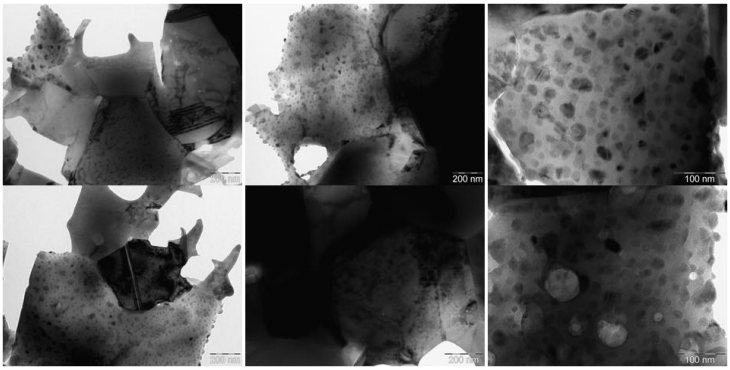

Figure 49: TEM images of the specimen obtained using a heating rate of 50°C/min and a holding time of 2 min at 900°C

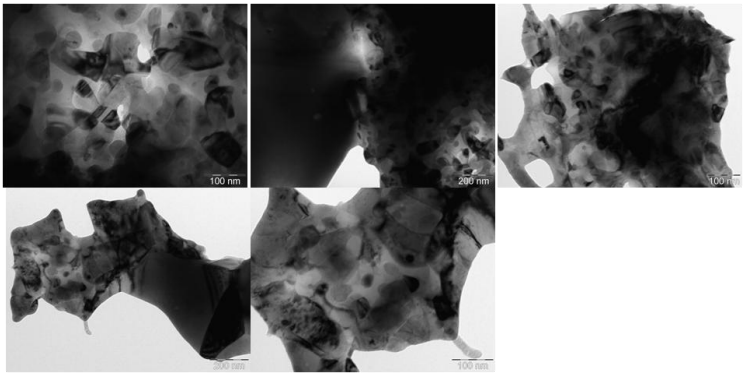

Figure 50: TEM images of the specimen obtained using a heating rate of 100°C/min and a 2 min holding time at 900°C

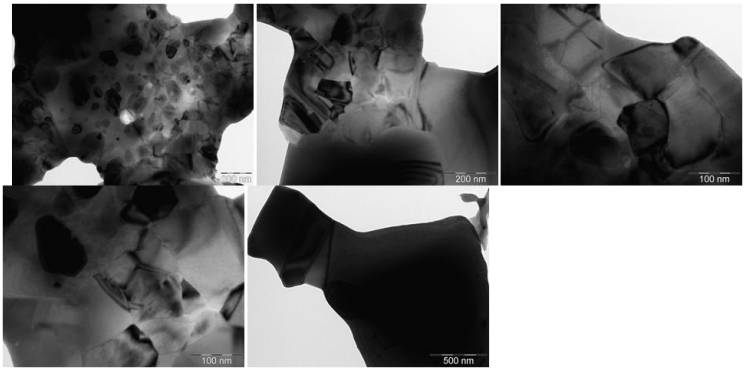

Figure 51: TEM images of the specimen obtained using a heating rate of 150°C/min and a 2 min holding time at 900°C

Large grains are embedded in nanostructured ones. At a heating rate of 150°C/min, only two representative structures are observed, which is not the case for lower heating rates characterized by an extra intermediate structure. In other words, on increasing heating rate the structure evolves towards a bimodal grain size distribution. The mean size of the nanometric grains is 55 ± 3 nm, in agreement with that obtained by XRD.

TEM ad EDAX analysis on the specimens indicates that the amount of oxide particles is greater in the finer (nano) grains (figure 52), confirming the effect of oxide particles on their stability.

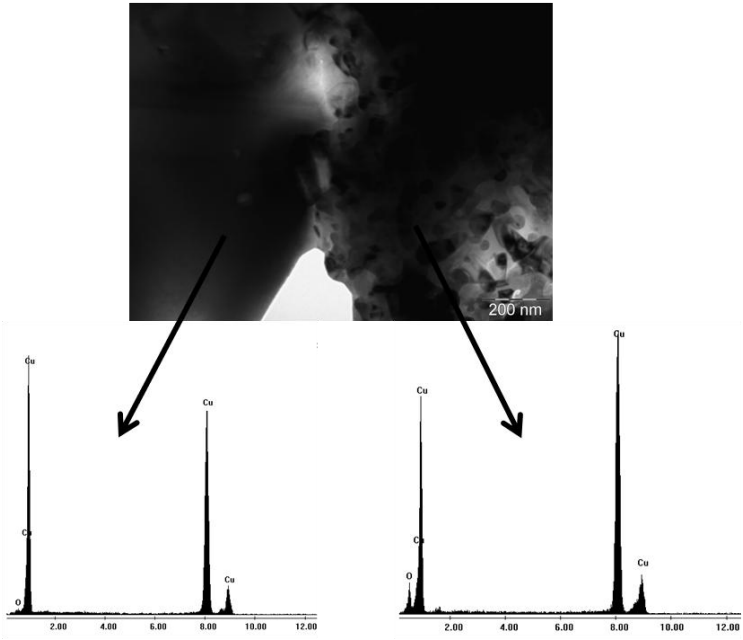

Figure 52: Oxygen analysis by EDAX

4.3.4. Tensile properties

As a final step of this work, a preliminary investigation on the tensile properties was carried out, and tensile specimens shown in Figure 53 were produced.

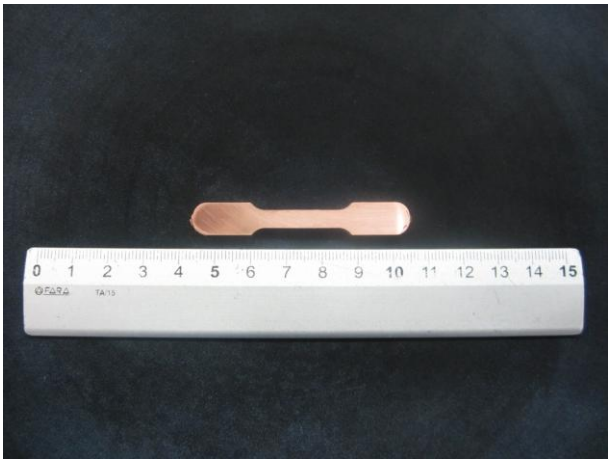

Figura 53: Tensile specimen used for the tensile tests

The specimens were produced with a 50°C/min heating rate and the holding time was varied (2, 5 and 10 min) in order to investigate its effect on density, grain size and tensile properties. and microstructure. It has to be mentioned that SPS is very sensitive to the geometry of the parts which are produced and therefore SPS of disks (previous case) and tensile testpieces (present case) in the same conditions may lead to different density and microstructure. The results presented here are the average of three specimens each condition.

Figure 54 shows three examples of the stress-strain curves obtained for the three holding times.

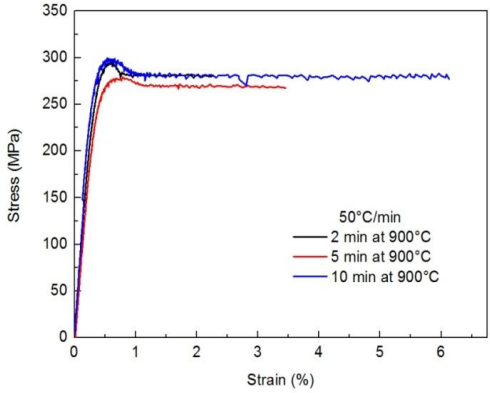

Figura 54: Tensile stress-strain curves of the sintered cryomilled copper at 50°C/min: effect of holding time

The stress-strain curves have a common shape: elastic deformation is followed by yielding and a maximum stress. They do not show the typical plastic instability of nanostructured metals, characterized by a continuous decrease of stress, but they show a plastic field with almost no strain hardening (Cheng S., 2005), with a plastic deformation reaching 6% in the specimen sintered 10 minutes. The absence of the plastic instability just after yielding has to be attributed to the fraction of ultrafine grains in the structure.

Tensile strength is quite high and tensile elongation increases with the holding time. Strength is very high, around 5 times higher than that of the atomized material. As expected, tensile ductility is much lower but it is comparable to that obtained by (Legros M, 2000) using mixtures of nano- and coarse powders.

Table 14 reports the results of the characterization and of tensile properties.

Tabella 14: Density, grain size and tensile properties as a function of holding time at the SPS temperature

Holding time (min)	Relative density (%)	Mean grain size (nm)	Yield Stress (MPa)	UTS (MPa)	Elongation at fracture (%)
2	96,8	38	301	309	2,0
5	95,3	48	279	286	2,2
10	96,6	81	283	289	3,1

The variation of density with holding time has a poor meaning, being comparable with the scatter of the results. Grain size increases slightly with holding time, as it might be expected, but it demonstrate that a given fraction of grains remain within the nanometric range. On increasing holding time strength decreases slightly and tensile elongation increases, accordingly.

As far as the grain size distribution in the nanometric range is concerned, Figure 55 shows an example relevant to the three holding times. Grain size distribution broaden on increasing holding time and shifts towards higher values.

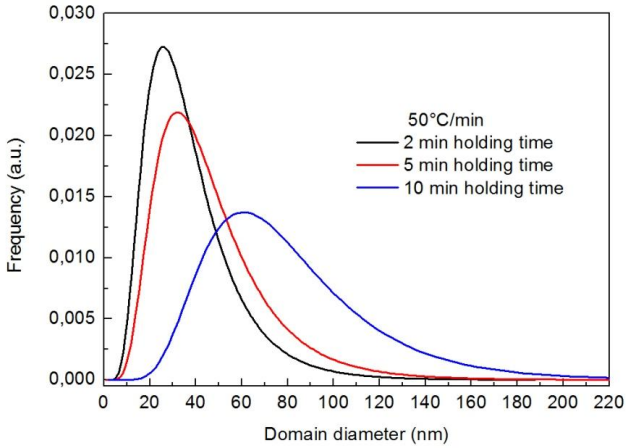

Figure 55: Effect of holding time on the crystalline domaine size distribution at a heating rate of 50°C/min

Figure 56 shows the fracture surface of the three specimens.

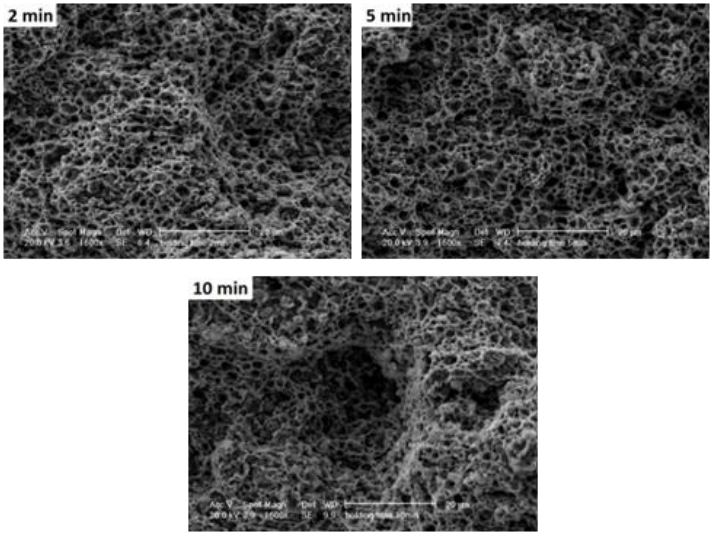

Figura 56: Fracture surface of the three specimens sintered at 50°C/min and at a holding time of 2, 5 and 10 min at 900°C

They show a dimpled morphology and several rounded particles within dimples, which are responsible for the nucleation of the ductile crack. No appreciable differences between the three morphologies can be appreciated.

4.3.5. Summary

From the investigation of the SPS of the cryomilled copper, the following conclusions can be derived:

1. Density increases with temperature and, in spite of the poor interaction between agglomerate size and temperature, temperature is slightly more effective on the fine agglomerates. Pressure and temperature have a

synergic effect on density and sintering is promoted increasing temperature .

2. The effect of nanostructure on Spark Plasma Sintering was also investigated by comparing the densification and sintering behavior of a cryomilled copper powder to that of the atomized powder (with the same mean particle size). The cryomilled powder was found to be more resistant to plastic deformation than the atomized one, but the huge density of dislocations and grain boundary activates sintering at low temperature. Densification is therefore promoted by deformation in the atomized powder and by sintering shrinkage in the cryomilled one. As a consequence, in the SPS conditions investigated the atomized specimen is densified but not sintered, while the cryomilled one is effectively sintered and consequently densified.
3. The contamination of the cryomilled powder gives rise to extensive degassing phenomena until 400°C which opposes densification, as demonstrated by the displacement rate of the lower punch during SPS. Therefore pressure has to be increased to the final value above this temperature, to favor densification.
4. When processed at the same nominal temperature (600°C) and pressure (6 MPa at the beginning of the SPS cycle, increased up to 20 MPa at the nominal temperature of 450°C) the cryomilled powder reaches a higher density than the atomized one. The cryomilled powder is effectively sintered but poorly deformed, while the atomized one is more extensively deformed but not significantly sintered.
5. The overheating profile of both atomized and cryomilled powders is very similar, even if resistivity of the cryomilled copper is much larger than that of the atomized one. The thickness of the overheated layer is much less than one micrometer in both cases. The different sintering behavior of the two powders may be attributed to the huge density of structural defects (dislocations and grain boundaries) within this layer, which activates mass transport phenomena responsible for neck formation and growth. In

particular the large density of dislocations may activate a dislocation pipe diffusion mechanism, since about 1% of atoms belong to dislocations in the cryomilled powder. The resulting effective lattice diffusion coefficient is two order of magnitude larger in the cryomilled powder, and activates sintering even at low temperature, as actually observed. The large density of grain boundary further contributes to activation of sintering and, in turn, of densification. Plastic deformation is the main densification mechanism in the atomized material; the great resistance to deformation of the cryomilled powder does not prevent densification which is promoted by the activation of sintering at much lower temperature.

6. The structure of the cryomilled specimens shows both nanometric and ultrafine grains, with a slight dependence on the heating rate, which tendencially increases grain size and its distribution. The effect of heating rate is fully canceled when the final pressure is applied at the sintering temperature. The application of pressure tends to increase dislocation density and grain size; this result has not been fully understood and will be subject of further investigation.
7. Tensile properties of the cryomilled specimens are much different from those f the atomized one: they show a greater strength and a significant ductility. Such a combination is due to the presence of both nanometric and ultrafine grains.
8. The increase in holding time at the sintering temperature does not affect density significantly and increases grain size and its distribution

Conclusions

The main results of the present PhD thesis may be summarized in the following points.

1. SPS mechanisms were investigated on an atomized copper powder through density measurement and fracture surface analysis. Rearrangement, local deformation, bulk deformation and sintering occurring successively on increasing temperature are the SPS mechanisms. These phenomena are enhanced by the great overheating of the particles surface layers in the contact regions. Densification does not necessarily imply sintering, the former may occur without the latter.

   The investigation of the effect of temperature, particle size and pressure on density and sintering has revealed the prevailing effect of temperature, followed by particle size and pressure, and temperature/particle size interaction effect is comparable to that of particle size. Temperature affects resistance to plastic deformation and the mass transport phenomena responsible for sintering, while particle size affects electrical resistance significantly and consequently the overheating profile. Moreover, particle size influences mass transport phenomena responsible for sintering through its effect on intraparticle grain size: the finer the particles, the larger the grain boundary surface, which results in an enhanced mass transport towards the neck region. The poor effect of pressure was believed to be due to the high deformability of copper.

To be more effective, the final pressure has to be applied at temperatures at which deformation propagates to the core of the particles. Within this range, the higher the temperature value at which pressure is increased the higher tensile ductility, while density and tensile strength are not influenced.

The surface overheating above the melting point of copper has been verified by SPS experiments on large copper particles (3 mm diameter) where the resolidified structure can be easily observed since overheating depth increases with particle size.

2. The nanostructured powder was produced by cryomilling the atomized copper powder for 8 h at a ball-to-powder ratio of 30:1. The structural characteristics of the milled powder were investigated through SEM, XRD and TEM. The powder, characterized by a mean crystallite size of 19±2 nm and a dislocation density of $6{,}25 \times 10^{16}$ m^{-2}, shows quite a great thermal stability. The high energy accumulated during the milling process was progressively released on increasing temperature along with the degassing of the powder, as a prerequisite step after which grain growth occures. On heating the interstitial oxygen reacts with copper forming oxide particles which exert grain boundary pinning, contributing to thermal stability. Thanks to its stability, the cryomilled powder maintain the nanostructure even after degassing at 300°C.
3. To highlight the effect of nanostructure, the sintering of both the cryomilled and atomized copper were compared. In the atomized copper densification is promoted by deformation and sintering occurs at high temperature; in the cryomilled powder sintering shrinkage is anticipated at much lower temperature due to its nanostructure. As aforementioned, temperature which is prevailing over particle size and pressure, is slightly more effective on the finer particle size. Pressure and temperature have a synergic interaction effect on density and sintering is promoted increasing temperature.

4. The increase in heating rate tends to increase grain size but this effect is canceled when the final pressure is applied at the sintering temperature; in this case, the final pressure tends to increase grain size and dislocation density, without any effect of heating rate.
5. The increase in holding time at the sintering temperature does not affect density significantly and increases grain size and expands its distribution
6. The sintered cryomilled specimens have a broad distribution of grain size, from the nanometric range up to the ultrafine one, as observed by combining XRD and TEM analyses. An increase in heating rate tends to promote a bimodal distribution of grain size.
7. Tensile tests were carried out on specimens produced in some selected conditions, an in particular by varying holding time at the sintering temperature. The tensile behavior is characterized by some plastic strain without an appreciable strain hardening; non plastic instability typical of nanostructured metals was observed. This is due to the presence of the ultrafine grains in the structure. The fracture surface shows a dimpled morphology, with evidence of the role of copper oxides on the ductile crack nucleation.
8. Tensile strength decreases and ductility increases on increasing holding time; in all the cases, they result in a good combination of strength and ductility. This result confirms that the bimodal distribution of grain size, which is necessary to provide an acceptable ductility to nanostructured metals, can be obtained by SPS.

The results of the present PhD thesis demonstrate the feasibility of the production of a nanostructured metal by cryomilling of atomized powders and Spark Plasma Sintering to obtain tensile properties with a promising combination of strength and ductility. Some points remain open and are the subject of further investigations.
The robustness of cryomilling has to be verified, since some variability in grain size and contamination of the cryomilled powder was observed even if cryomilling was carried out in the same conditions.

Sintered density of the cryomilled specimens produced in this work was never 100% of the theoretical one. According to my opinion, full densification may be obtained by increasing pressure but this couldn't be verified due to technical limitations of the apparatus available. In this case, the effect of the increased pressure on grain size and dislocation density has to be verified, and the combined effect of improved density and the expected structural modification on tensile properties has to be investigated.

As a further point, the robustness of SPS should be verified, too.

Publications

1. S. Diouf, C. Menapace and A. Molinari. Study of the effect of particle size on densification of copper during spark plasma sintering. **Powder Metallurgy, 55 (3) (2012) 228-234**
2. S. Diouf, A. Molinari. Densification mechanisms in spark plasma sintering: Effect of particle size and pressure. **Powder Technology 221 (2012) 220-227**
3. A. Molinari, S. Libardi, L. Maines, S. Diouf. Effect of heating rate on Spark Plasma Sintering of nanostructured Fe-Mo powders**. Int. J. Powder Metall., 48 (6) (2012) 31-39.**
4. S. Diouf, C. Menapace, A. Molinari. Spark Plasma Sintering of cryomilled copper powder (**submited**)
5. S. Diouf, A. Fedrizzi, A. Molinari. A fractographic and microstructural analysis of the neck regions of coarse copper particles consolidated by Spark Plasma Sintering (**submited**)

6. S. Diouf, Molinari A. A Differential Scanning Calorimetry (DSC) study of the thermal stability of cryomilled copper powder (**in preparation**)
7. S. Diouf, Molinari A. Mechanical properties of spark plasma sintered cryomilled copper (**in preparation**)

Conferences

8. S. Diouf, C. Menapace and A. Molinari., Spark Plasma Sintering of copper powders with different particle sizes, presented to EUROMAT, 12-15 September 2011, Montpellier, France
9. S. Diouf, A. Molinari. Spark Plasma Sintering of Cryomilled Copper. Proceedings EURO PM2012 Congress Exhibition, Basel 16-19 September 2012, ed. EPMA, Shrewsbury (UK), vol. 1, pp. 11-16.
10. A. Molinari, S. Diouf. Spark Plasma Sintering mechanism of nanostructured copper powder. Proceedings PM2012, Japan, 14 - 18 October 2012, ed. PM

Bibliography

Anselmi-Tamburini U. Gennari S., Garay J. E. and Munir Z. A. Fundamental investigations on the spark plasma sintering/synthesis process: II. Modeling of current and temperature distributions. Mater Sci Eng A, **2005**. 394: p. 139-148.

Anselmi-Tamburini U. Spinolo G., Maglia F., Tredici I., Holland T.B., Mukherjee A. K. Field Assisted Sintering Mechanisms. Engineering Materials . **2013**. 35: p. 159-193.

Bernard-Granger G. Guizard C. Densification mechanism involved during spark plasma sintering of a codoped a-alumina material: Part I. Formal sintering analysis. J. Mater. Res. **2009**. 24(1): p. 179–186.

Chen X.J. Khor K.A., Chan S.H., Yu L.G. Overcoming the effect of contaminant in solid oxide fuel cell (SOFC) electrolyte: spark plasma sintering (SPS) of 0.5wt.%

silica-doped yttria-stabilized zirconia (YSZ). Materials Science and Engineering A. **2004**. 374: p. 64–71.

Cheng S. Ma E., Wang Y.M., Kecskes L.J., Youssef K.M., Koch C.C., Trociewitz U.P., Han K. Tensile properties of in situ consolidated nanocrystalline Cu. Acta Mater . **2005**. 53(5): p. 1521-1533.

Dao M. Lu L., Asaro R.J., De Hosson J.T.M., Ma E. Toward a quantitative understanding of mechanical behavior of nanocrystalline metals. Acta Materialia. **2007** . 55(12): p. 4041-4065.

Dorbolo S. Ausloos M. and Vandewalle N. Reexamination of the Branly effect. Physical Review E. **2003**. 67: p. 040302 (R) .

Dorbolo S. Merlen A., Creyssels M., Vandewalle N., Castaing B. and Falcon E. Effects of electromagnetic waves on the electrical properties of contacts between grains. Europhysics Letters. **2007**. 79: p. 54001.

El-Tantawy Farid. New double negative and positive temperature coefficients of conductive EPDM rubber TiC ceramic composites. European Polymer Journal . **2002**. 38: p. 567–577.

Eric Falcona, Bernard Castaing. Electrical conductivity in granular media and Branly's coherer: A simple experiment. Am. J. Phys. **2005**. 73(4): p. 302-307.

Gleiter H. Nanostructured materials: basic concepts and microstructure. Acta Mater. **2000**. 48: p. 1-29.

Grosdidier T. Goran D., Ji G. and Llorca N. On the processing of hetero-nanostructured metals for improved strength/ductility balance by ECAE and SPS techniques. Journal of Alloys and Compounds. **2010**. 504S: p. S456–S459.

Groza J. R. Garcia M. and Schneider J. A. Surface effects in field-assisted sintering. J.Mater. Res. **2001**. 16(1): p. 286-292.

Guo Shu-Qi Nishimura T., Kagawa Y., and Yang JM. Spark Plasma Sintering of Zirconium Diborides. J. Am. Ceram. Soc. **2008**. 91(9): p. 2848–2855.

Guyot P. Rat V., Coudert J. F., Jay F., Maıtre A. and Pradeilles N. Does the Branly effect occur in spark plasma sintering? Journal of Physics D: Applied Physics. **2012**. 45: p. 092001.

Hayes R.W. Rodriguez R. and Lavernia E.J. The mechanical behavior of a cryomilled Al–10Ti–2Cu alloy. Acta Mater. 2001. 49: p. 4055–4068.

Hill R. E. Reed. Physical Metallurgy Principles. **2009**, Stamford (CA) : Cengage Lerning, 4th edition: p. 268-272.

Holland T.B. Ovid'ko I.A., Wang H., Mukherjee A.K. Elevated temperature deformation behavior of spark plasma sintered nanometric nickel with varied grain size distributions. Materials Science and Engineering A. **2010**. 528: p. 663–671.

Hulbert D. M. Anders A., Andersson J., Lavernia E. J. and Mukherjee A. K. A discussion on the absence of plasma in spark plasma sintering. Scripta Materialia. **2009**. 60: p. 835-838.

Hungría T. Galy J., Castro A. Spark Plasma Sintering as a Useful Technique to the Nanostructuration of Piezo-Ferroelectric Materials. Advanced Engineering Materials. **2009** . 11(8): p. 615-631.

Johnson K. L. Contact Mechanics. 1985, Cambridge, Cambridge University Press: p. 432–447.

Kim C. K. Lee S., Shin S.Y., Kim D.H. Effects of consolidation temperature and pressure on microstructures and mechanical properties of Cu-based bulk amorphous alloys consolidated by spark plasma sintering. Journal of Alloys and Compounds. **2008**. 453: p. 108-114.

Koch C.C. Morris D.G., Lu K. and Inoue A. Mater Res Soc Bull . 1999. 24: - p. 54.

Koch C.C. Structural nanocrystalline materials: an overview. J Mater Sci . **2007**. 42(5): p. 1403-1414.

Kodash V.Y. Groza J.R., Cho K.C., Klotz B.R., and Dowding R.J. Field-assisted sintering of Ni nanopowders. Materials Science and Engineering A. **2004**. 385(1-2): p. 367–371.

Kumar K.S. Van Swygenhoven H., Suresh S. Mechanical behavior of nanocrystalline metals and alloys. Acta Materialia. **2003**. 51(19): p. 5743-5774.

Langer J. Hoffmann M. J., Guillon O. Direct comparison between hot pressing and electric field-assisted sintering of submicron alumina. Acta Materialia. **2009**. 57: p. 5454–5465.

Lavernia E.J. Han B.Q., Schoenung J.M. Cryomilled nanostructured materials: Processing and properties. Materials Science and Engineering A. **2008**. 493: p. 207-214.

Lee Z. Rodriguez R., Hayes R.W., Lavernia E.J. and Nutt S.R. Microstructural Evolution and Deformation of Cryomilled Nanocrystalline Al-Ti-Cu Alloy. Metall. Mater. Trans. A. **2003**. 34(7): p. 1473–1481.

Legros M Elliot BR, Rittner MN, Weertman JR, Hemker KJ. Microsample tensile testing of nanocrystalline metals. Phil. Mag. A. **2000**. 80: p. 1017.

Leoni M. Confente T. and Scardi P. PM2K: a flexible program implementing Whole Powder Pattern Modelling. Z. Kristallogr. Suppl. **2006**. 23: p. 249 - 254.

Li B.R. WangX.H., Cai M.M., Hao L.F., Li L. Densification of uniformly small-grained BaTiO3 using spark-plasma-sintering. Mater. Chem. Phys. **2003**. 82: p. 173-180.

Libardi S. Leoni M., Facchini L., D'Incau M., Scardi P. and Molinari A. Effect of the dispersion of nanometric silica particles on the thermal stability of a nanostructured iron based powder. Mater Sci Eng A. **2007**. 445-446: p. 244-250.

Liu D. Xiong Y., , Li Y., Topping T. D., Zhou Y., Heines C., Paras J., Martin D., Kapoor D., Schoenung J. M. and Lavernia E. J. Spark Plasma Sintering of cryomilled nanocrystalline Al alloy – Part II: Influence of processing conditions on densification and properties. Metallurgical and Materials Transactions A. **2012**. 43: p. 340-350.

Locci A.M. Cincotti A., Todde S., Orrù R. and Cao G. A methodology to investigate the intrinsic effect of the pulsed electric current during the spark plasma sintering of electrically conductive powders. Sci. Technol. Adv. Mater. 2010. 11: p. 045005.

Lu K. Sintering of nanoceramics. Int. Mater. Rev. 2008. 53(1): p. 21–38.

Luton M. J. Jayanth C. S., Disko M. M., Matras S. and Vallone J. Cryomilling of Nano-Phase Dispersion Strengthened Aluminum. MRS Proceedings. **1988**. 132: p. 79. - doi:10.1557/PROC-132-79.

Lutterotti L. Matthies S., Wenk H.R., Schultz A.S., Richardson J.W.Jr. Combined texture and structure analysis of deformed limestone from time-of-flight neutron diffraction spectra. J. Appl. Phys. 1997. 81: p. 594.

M.Tokita. Mechanism of Spark Plasma Sintering. Sumitomo Coal Mining Company, Internal Comunication . p. 13 pp..

Ma E. Instabilities and ductility of nanocrystalline and ultrafine-grained metals. Scripta Materialia. –**2003**. 49: p. 663–668.

Mamedov V. Spark plasma sintering as advanced PM sintering method. Powder Metall. 2002. 45(4): p. 322–328.

McWilliams B. Zavaliangos A., Cho, Robert K.C., Dowding J. The modeling of electric-current-assisted sintering to produce bulk nanocrystalline tungsten. JOM. **2006**. 58: p. 67.

Meyers M.A. Mishra A., Benson D.J. Mechanical properties of nanocrystalline materials. Progress in Materials Science. **2006**. 51: p. 427–556.

Misawa T. Shikatani N., Kawakami Y., Enjoji T., Ohtsu Y., Fujita H. Observation of internal pulsed current flow through the ZnO specimen in the spark plasma sintering method. J Mater Sci . **2009**. 44: p. 1641–1651.

Moelle C. H. and Fecht H. J. Thermal stability of nanocrystalline iron prepared by mechanical attrition. Nanostructured Materials. **1995**. 6: p. 421-424.

Molinari A. Libardi S., Leoni M. and Scardi P. Role of lattice strain on thermal stability of a nanocrystalline FeMo alloy. Acta Materialia. **2010**. 58: p. 963–966.

Molinari A. Libardi S., Maines L., Diouf S. Effect of heating rate on Spark Plasma Sintering of nanostructured Fe-Mo powders. Int. J. Powder Metall. **2012**. 48(6): p. 31-39.

Molinari A. Lonardelli I., Demetrio K., Menapace C. Effect of the particle size on the thermal stability of nanostructured aluminum powder: dislocation density and second-phase particles controlling the grain growth. J. Mater. Sci. 2010. 45(24): p. 6739-6746.

Mouawad B. Soueidan M., Fabrègue D., Buttay C., Bley V., Allard B., Morel H. Full densification of Molybdenum powders using Spark Plasma Sintering. Metallurgical & Materials Transactions. Part A. **2012**. 43(9): p. 3402-3409.

Mukherjee A.K. An examination of the constitutive equation for elevated temperature plasticity. Mater Sci Eng A. **2002**. 322: p. 1-22.

Munir Z. A. Anselmi-Tamburini U. and Ohyanagi M. The effect of electric field and pressure on the synthesis and consolidation of materials: A review of the spark plasma sintering method. J. Mater. Sci. 2006. 41(3): p. 763-777.

Munir Z. A. Anselmi-tamburini U., Ohyanagi M. The effect of electric field and pressure on the synthesis and consolidation of materials: A review of the spark plasma sintering method. J. Mater. Sci. 2006. 41: p. 763-777.

Olevski E. Froyen L. Constitutive modeling of spark-plasma sintering of conductive materials. Scripta mater. 2006. 55: p. 1175-1178.

Olevsky E. A. Kandukuri S., and Froyen L. Consolidation enhancement in spark-plasma sintering: Impact of high heating rates. J. Appl. Phys. **2007**. 102: p. 114913.

Olevsky E. Froyen L. Constitutive modelling of spark plasma sintering of conductive materials. Scripta Materialia. **2006**. 55: p. 1175-1178.

Omori M. Sintering, consolidation, reaction and crystal growth by the spark plasma system (SPS). Mater Sci Eng A . **2000**. 287: p. 183-188.

Orrù R. Licheri R., Locci A. M., Cincotti A., and Cao G. Consolidation/synthesis of materials by electric current activated/assisted sintering. Mater. Sci. Eng. R. **2009**. 63: p. 127–287.

Ovid'ko I. A. Review on the fracture processes in nanocrystalline materials. J Mater Sci . **2007**. 42(5): p. 1694-1708.

Ovid'ko I.A. Langdon T.G. Enhanced ductility of naocrystalline and ultrafine-grained metals. Rev. Adv. Mater. Sci. **2012**. 30: p. 103-111.

Perez R.J. Jiang H.G., Dogan C.P. and Lavernia E.J. Grain Growth of Nanocrystalline Cryomilled Fe-Al Powders. Metall. Mater. Trans. A. **1998**. 29: p. 2469-2475.

Prasad Y.V.R.K. Rao K.P. Influence of oxygen on rate-controlling mechanisms in hot deformation of polycrystalline copper: oxygen-free versus electrolytic grades. Materials Letters. **2004**. 58(14): p. 2061-2066.

Risbud S.H. Groza J.R. & Kim M.J. Clean grain boundaries in aluminium nitride ceramics densified without additives by a plasma-activated sintering process. Phil. Mag. B. **1994**. 69(3): p. 525-533.

Ritasalo R. Cura M. E., Liu X. W., Söderberg O., Ritvonen T. and Hannula S. P. Spark plasma sintering of submicron-sized Cu-powder Influence of processing parameters and powder oxidization on microstructure and mechanical properties. Mater Sci Eng A. **2010**. 527: p. 2733-2737.

Roy I. Chauhan M., LAVERNIA E. J. and Mohamed F. A. Thermal Stability in Bulk Cryomilled Ultrafine-Grained 5083 Al Alloy. METALLURGICAL AND MATERIALS TRANSACTIONS A. **2006**. 37: p. 721-730.

Sakka Y. Reduction and sintering of ultrafine copper powders. Journal of Materials Science Letters. **1989**. 8: p. 273-276.

Sanders P.G. Eastman J.A., Weertman J.R. Elastic and tensile behavior of nanocrystalline copper and palladium. Acta Materialia. **1997**. Vol. 45(10): p. 4019-4025.

Sanders P.G. Youngdahl C.J., Weertman J.R. The strength of nanocrystalline metals with and without flaws. Mater. Sci. Eng. A. **1997**. 234-236: p. 77-82.

Sergueeva A.V. Mara N.A., Mukherjee A.K. Deformation Mechanisms in a Nanocrystalline Vitroperm Alloy. Rev. Adv. Mater. Sci. **2004**. 7(2): p. 67-74.

Shewmon P. Diffusion in Solids. 1989. Warrendale (PA) : The Minerals, Metals and Materials Society..2nd edition. p. 202-205.

Shima Y. Ishikawa Y., Nitta H., Yamazaki Y., Mimura K., Isshiki M. and Iijia Y. Self-diffusion along dislocations in ultra high purity iron. Materials Transactions. **2002**. 43(2): p. 173-177.

Siddiqui R. A. Alp T. Effect of isothermal annealing on the Bordoni relaxation in cold worked copper. J. Mater. Sci. **1991**. 26: p. 6362-6372.

Siegel R.W. Fougere G.E. Mechanical properties of nanophase metal. Nanostruct. Mater. **1995**. 6: p. 205-216.

Simões S. Calinas R., Vieira M. T., Vieira M. F. and Ferreira P. J. In situ TEM study of grain growth in nanocrystalline copper thin films. Nanotechnology. **2010**. 21: p. 145701.

Sobol' V. R. Logvinovich P. N., Bel'skii S. E. and Blokhin A. V. Temperature mechanisms of the interaction of dislocations with impurities in the processes of transfer of the energy of elastic vibrations. Journal of Engineering Physics and Thermophysics. **2007**. 80(4): p. 840-846.

Song X. Liu X. and Zhang J. Neck Formation and Self-Adjusting Mechanism of Neck Growth of conducting powders in Spark Plasma Sintering. J. Am. Ceram. Soc. **2006**. 89(2): p. 494-500.

Srinivasarao B. Oh-ishi K., Ohkubo T., Mukai T. and Hono K. Synthesis of high-strength bimodally grained iron by mechanical alloying and spark plasma sintering. Scripta Mater. 2008. 58: p. 759-762.

Srinivasarao B. Suryanarayana C., Oh-ishi K. and Hono K. Microstructure and mechanical properties of Al-Zr nanocomposite materials. Materials Science and Engineering A. **2009**. 518(1-2): p. 100–107.

Suryanarayana C. Koch C.C. Nanocrystalline materials – Current research and future directions. Hyperfine Interactions. **2000**. 130(1-4): p. 5-44.

Suryanarayana C. Mechanical alloying and milling [Rivista] // Prog. Mater. Sci.. - **2001**. 46: p. 1-184.

Team R Development Core. R: a language and environment for statistical computing. R Foundation for Statistical Computing. **2010**. Vienna .

Tellkamp V. L. Melmed A. and Lavernia E.J. Mechanical Behavior and Microstructure of a Thermally Stable Bulk Nanostructured Al Alloy, Metall. Mater. Trans. A. **2001.** 32: p. 2335-2343.

Tiwari D. Basu B., Biswas K. Simulation of thermal and electric field evolution during spark plasma sintering. Ceramics International. **2009**. 35: p. 699-708.

Tokita M. Development of Large-Size Ceramic/Metal Bulk FGM Fabricated by Spark Plasma Sintering. Mater Sci Forum. **1999**. 308-311: p. 83-88.

Valiev R. Z. Islamgaliev R.K. and Alexandrov I. V. Bulk nanostructured materials from severe plastic deformation. Prog. Mater. Sci. **2000**. 45. - p. 103-189.

Vanmeensel K. Laptev A., Hennicke J., Vleugels J., Van der Biest O. Modelling of the temperature distribution during field assisted sintering. Acta Materialia. **2005**. 53: p. 4379–4388.

Wang S.W. Chen L.D., and Hirai T. Densification of Al2O3 powder using spark plasma sintering. J. Mater. Res. **2000**. 15(4): p. 982-987.

Wang Y. Chen M., Zhou F., Ma E. High tensile ductility in a nanostructured metal. Nature. **2002**. 419 912-915.

Wang Y. Fu Z. Study of temperature field in spark plasma sintering. Mater. Sci. Eng. B. **2002**. 90: p. 34 .

Wang Y. M. Ma E. Enhanced tensile ductility and toughness in nanostructured Cu. Appl. Phys. Lett. **2002**. 80(13):.p. 2395-2397.

Wang Y.M. Ma E. Three strategies to achieve uniform tensile deformation in a nanostructured metal. Acta Materialia. **2004**. 52(6): p. 1699–1709.

Wen H. Zhao Y., Zhang Z., Ertorer O., Dong S. and Lavernia E. J. The influence of oxygen and nitrogen contamination on the densification behavior of cryomilled copper powders during spark plasma sintering. Journal of Materials Science. **2011**. 46(9): p. 3006-3012.

Wolf D. Yamakov V., Phillpot S.R., Mukherjee A., Gleiter H. Deformation of nanocrystalline materials by molecular-dynamics simulation: relationship to experiments? Acta Materialia. **2005**. 53(1): p. 1-40.

Xiong Y. Liu D., Li Y., Zheng B., Heines C., Paras J., Martin D., Kapoor D., **Lavernia E. J. and Schoenung J. M.** Spark Plasma Sintering of cryomilled nanocrystalline Al alloy – Part I: Microstructure Evolution. Metallurgical and Materials Transactions A. **2012**. 43: p. 327-339.

Yanagisawa O. Kuramoto H., Matsugi K. and Komatsu M. Observation of particle behavior in copper powder compact during pulsed electric discharge. Materials Science and Engineering A. **2003**. 350: p. 184-189.

Ye J. Ajdelszajn L., Scoenhung J.M. Bulk nanocrystalline aluminum 5083 alloy fabricated by a novel technique: cryomilling and spark plasma sintering. Metall. Mater. Trans. A. **2006**. 37: p. 2569.

Zadra M. Casari F., Girardini L. and Molinari. A Spark plasma sintering of pure aluminium powder: mechanical properties and fracture analysis. Powder Metallurgy. 2007. 50(1): p. 40-45.

Zavaliangos A. Zhang J., Krammer M., Groza J.R. Temperature evolution during field activated sintering. Materials Science and Engineering A. 2004. 379: p. 218–228.

Zhang X. Wang H. and Koch C. C. Mechanical behavior of bulk ultrafine-grained and nanocrystalline Zn. Rev. Adv. Mater. Sci. 2004. 6: p. 53-93.

Zhang Z. H. Wang F. C., Lee S. K., Liu Y., Cheng J. W., Liang Y. Microstructure characteristic, mechanical properties and sintering mechanism of nanocrystalline copper obtained by SPS process. Mater Sci Eng A. 2009. 523: p. 134-138.

Zhang Z. H. Wang F. C., Wang L. and Li S. K. Ultrafine-grained copper prepared by spark plasma sintering process. Materials Science and Engineering A. **2008**. 476. p. 201-205.

Zhao Y. H. Lu K. Microstructure evolution and thermal properties in nanocrystalline Cu during mechanical attrition. Physical Review B. **2002**. 66: p. 085404.

Zhaohui Z Fuchi W., Lin W., Shukui L., Osamu S. Sintering mechanism of large-scale ultrafine-grained copper prepared by SPS method. Materials Letters. **2008**. 62(24): p. 3987–3990.

Zhao-Hui Z. Fu-Chi W., Lin W., and Shu-Kui L. Ultrafine-grained copper prepared by spark plasma sintering process. Mater Sci Eng A. **2008**. 476: p. 201-205.

Zhou F. Liao X.Z., Zhu Y.T., Dallek S. and Lavernia E.J. Microstructural evolution during recovery and recrystallization of a nanocrystalline Al-Mg alloy prepared by cryogenic ball milling. Acta Mater. **2003**. 51: p. 2777-2791.

Zúñiga A. Ajdelsztajn L., and Lavernia E.J. Spark Plasma Sintering of a Nanocrystalline Al-Cu-Mg-Fe-Ni-Sc Alloy. Metall. Mater. Trans. A. **2006**. 37(4): p. 1343–52.

Acknowledgments

I would like to thank professor Alberto Molinari for his guidance, trust, patience, and invaluable support. and Mario Zadra for the SPS experiments and invaluable discussions.

Special thanks to Dr. Mirco D'Incau (UniTN) for XRD experiments, Dr. Gloria Ischia and Dr. Lorena Maines for TEM and SEM analysis, Wilma vaona for her assistance with thermal analysis.

Special thanks to my colleagues in Laboratorio di Metallurgia for their friendship and for making this PhD duration a great experience. Special thanks to Dr. Cinzia Menapace, Dr. Anna Fedrizzi and Prof. Ilaria Cristofolini.

Special thanks to Prof. Djibril Diop, Prof. Giuseppe Dalba, Roberto Graziola and all my colleagues in Lux Laboratory (UCAD, Dakar) for their ever lasting support.

Last but not least, my parents and wife for their patience and support.